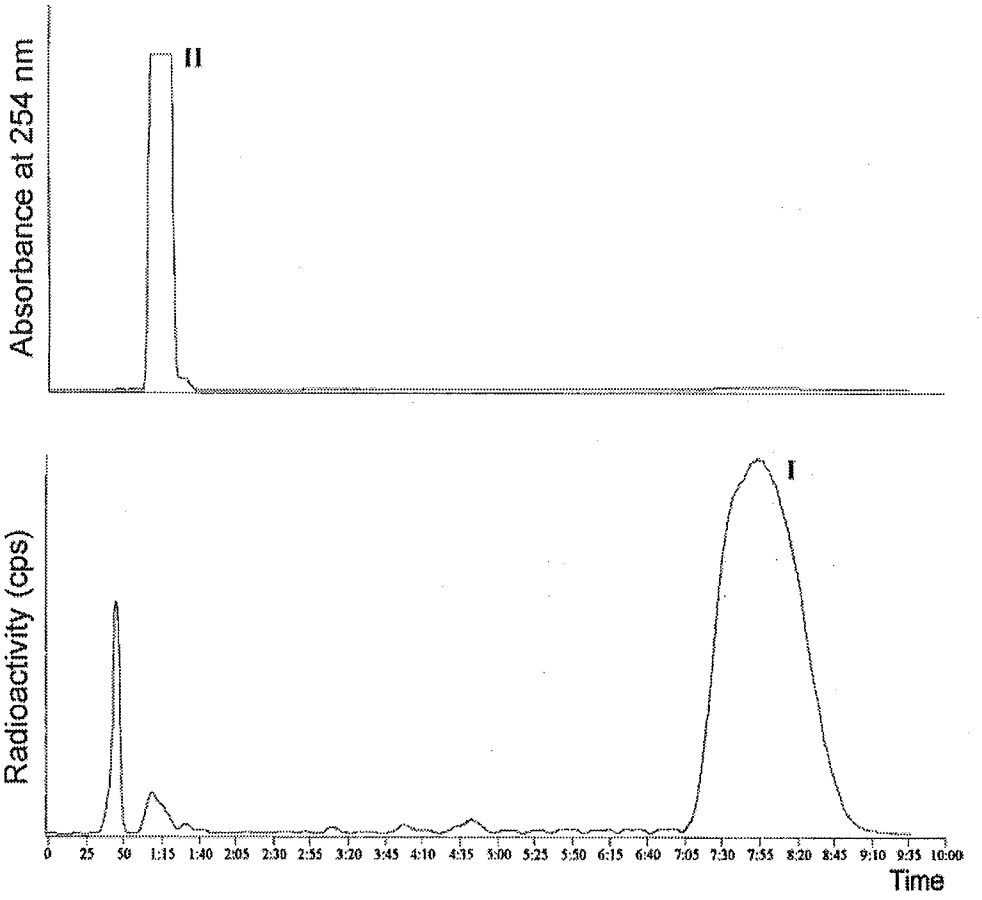


**Fig. 3.** Semi-preparative HPLC chromatograms (u.v. and radioactivity vs time) using a semi-preparative reversed phase HPLC column. *I*, [$^{11}$C]PE2I; *II*, PE2I acid precursor

*PET measurements in monkeys.* Four cynomolgus monkeys weighing about 4 kg were supplied by the National Institute for Infectious Diseases, Solna, Stockholm. Anaesthesia was induced by repeated i.m. injection of ketamine (Ketalar 10–15 mg kg$^{-1}$ h$^{-1}$). A head fixation system was used to secure a fixed position of the monkey head during the PET measurements [34]. The monkey head was positioned so that the imaging planes were parallel to the canthomeatal line. Body temperature was controlled by a heating pad with a thermostat. In each PET study, 44–53 MBq of [$^{11}$C]PE2I was injected i.v. in the left sural vein. Radioactivity in brain was measured according to a pre-programmed sequence of frames up to 118 min after injection.

Altogether 11 PET measurements were performed in the monkeys. In each monkey a baseline measurement was performed. In the first monkey, five PET measurements were performed on two experimental days. On the first experimental day a baseline measurement was followed by a displacement measurement, in which β-CIT (0.5 mg/kg) was injected i.v. 21 min after the injection of [$^{11}$C]PE2I. On the second experimental day 2 weeks later, a baseline measurement was followed by a displacement measurement in which cocaine (2 mg/kg) was injected i.v. 21 min after the injection of [$^{11}$C]PE2I. The day ended with a pretreatment measurement, in which cocaine (2 mg/kg) was injected i.v. 5 min before the injection of [$^{11}$C]PE2I.

Two measurements were performed on the same day in the second monkey. The first was a baseline measurement. The second was a pretreatment measurement in which the selective dopamine transporter GBR 12909 (5 mg/kg) [35] was injected i.v. 8 min before the injection of [$^{11}$C]PE2I.

Two measurements were performed in the third monkey. The first was a baseline measurement. The second was a pretreatment measurement in which the selective noradrenaline transporter maprotiline (5 mg/kg) [36] was injected i.v. 5 min before the injection of [$^{11}$C]PE2I.

Two measurements were performed in the fourth monkey. The first was a baseline measurement. The second was a pretreatment measurement in which the selective serotonin transporter citalopram (5 mg/kg) [37] was injected i.v. 5 min before the injection of [$^{11}$C]PE2I.

Venous blood samples (2 ml) were obtained at about 4, 15, 30. and 45 min after the injection of [$^{11}$C]PE2I for metabolite measurements.

*PET measurements in a healthy human subject.* The study was performed in compliance with the Declaration of Helsinki and approved by the Ethics and Radiation Safety committees of the Karolinska Hospital, Stockholm. One male subject (age 30 years, weight 78 kg) participated after giving informed consent. The subject was healthy according to history, physical examination, blood and urine chemistry and a magnetic resonance imaging (MRI) examination of the brain.

An individualised plaster helmet was made for the subject and used with a head fixation system during both MRI and PET [38]. One venous cannula was inserted into the brachial artery of the left arm and one venous cannula was inserted into the antecubital vein of the right arm. [$^{11}$C]PE2I (293 MBq) was injected i.v. as a bolus during 2 s into the right antecubital vein. The PET measurement comprised a series of sequential frames during 68 min.

Blood samples (2 ml) were obtained at 4, 10, 20, 30, 40, 50 and 60 min after injection of [$^{11}$C]PE2I for metabolite measurements. Blood was drawn from the arterial cannula and radioactivity in blood was measured using a well counter [39]. Blood samples (2 ml) were drawn manually at each time frame until the end of the experiment. One millilitre of the blood sample was immediately pipetted and radioactivity was measured in a well counter for 10 s. After centrifugation of the remaining blood sample, 0.2 ml plasma was pipetted and plasma radioactivity was measured in the well counter. Radioactivity in whole blood and plasma was corrected for decay and plotted versus time.

*Plasma metabolite studies.* The fractions of radioactivity in monkey and human plasma that corresponded to unchanged [$^{11}$C]PE2I and labelled metabolites were determined using an HPLC method previously developed for other PET ligands [40]. The supernatant (0.5 ml) obtained after centrifugation at 2,000 *g* for 1 min of the blood samples (2 ml) was mixed with acetonitrile (0.7 ml) containing a standard of PE2I. The radioactivity in the supernatant (1.1 ml) obtained after centrifugation at 2,000 *g* for 1 min was measured in the well counter (extraction yield >95%) and 1 ml was subsequently injected into the HPLC column. The mixture was chromatographed through the column and the UV-absorption and radioactivity peaks were integrated and the data were stored in a PC.

The reversed-phase HPLC Kontron system consists of: 2 Kontron 420 pumps, a Rheodyne injector (7125 with a 1.0-ml loop) equipped with a Waters μ-Bondapak-C18 column (300×7.8 mm, 10 μm) and a Kontron 432 UV-spectrophotometer (254 nm) in series with a Packard Radiochromatography detector Serie A-100 (1 ml cell). Phosphoric acid (0.01 *M*) (A) and acetonitrile (B) were used as the mobile phases with a flow rate of 6.0 ml/min. Gradient elution was employed on all metabolite analyses. The gradient profile was the following: HPLC time 0–5.5 min, (A/B) 80/20–40/60; 5.5–6.0 min, (A/B) 40/60–80/20; 6.0–7.5 min, (A/B) 80/20 isocratic; 8.5 min end. The Kontron 450 Multitasking system was used as an efficient controller and PC-integration system. Fractions that correlated with standards of PE2I and the corresponding radioactive peaks were also taken and counted in a well counter. The radioactivity in a certain fraction was divided by the total radioactivity and expressed as a percentage of the total.

*Regions of interest (ROIs).* In monkeys, the ROIs were drawn on the PET summation images representing radioactivity measured from 9 min after i.v. injection to the end of the measurement. The striatum, substantia nigra, neocortex, cerebellum and the whole brain contour were defined according to an atlas of a cryosected cynomolgus monkey head in situ. Radioactivity was calculated for the sequence of time frames, corrected for the radioactivity decay and plotted versus time.

To calculate the percentage of [$^{11}$C]PE2I injected that was present in brain at the time of maximal radioactivity, the radioactivity concentration in the ROI for the whole brain was multiplied by the estimated brain volume of 65 ml for a cynomolgus monkey weighing 4 kg. The calculated value for total radioactivity in brain was then divided by the radioactivity injected and multiplied by 100 to obtain the percentage.

In the human subject, ROIs were delineated manually on the MR images according to the anatomical boundaries for the putamen, the caudate nucleus, the substantia nigra, the frontal cortex and the cerebellum. The ROIs were transferred to the corresponding PET images. Regional radioactivity was measured for each sequential scan, corrected for $^{11}$C decay and plotted versus time. The percent of radioligand in brain was calculated as described above for the monkey brain. The estimated average brain volume of a healthy male was 1,250 ml.

*Quantitative analyses.* The cerebellum is a region with negligible density of DAT [27, 41]. The radioactivity in the cerebellar cortex was therefore used as an approximation for free and non-specifically bound radioligand concentration in brain. To validate the assumption that the radioactivity in the cerebellum can be used as an estimate of the time curve for free and non-specifically bound radioligand concentration in brain, the time curve for the ratio of radioactivity in cerebellum to blood was calculated for [$^{11}$C]PE2I in each pair of baseline and pretreatment measurements.

The time curve for specific [$^{11}$C]PE2I binding to DAT in the putamen and the thalamus was defined as the difference between the total radioactivity concentration in an ROI and the cerebellum. Time for peak equilibrium was defined as the moment when the curve for specific binding reached a peak [42].

The ratio of binding in an ROI to the cerebellum was calculated using the time intervals 55–65 min in monkeys and 40–50 min in man, at which peak equilibrium occurred. This ratio corresponds to the binding potentials and can be viewed as an index of the density of available receptors. All calculations were based on the assumption that radioactivity in brain represents unchanged radioligand [43].

*Volume rendering.* The distribution of the dopamine transporter in the monkey and human brain was also visualised using a volume rendering technique. The technique was developed by Pixar Inc, USA and was described in a pioneering paper by Drebin et al. [44]. The technique has previously been applied to PET data to visualise [$^{11}$C]flumazenil binding to benzodiazepine receptors in the human brain [45].

The basic concept in volume rendering is that each volume element, voxel, representing radioactivity uptake in the brain is projected onto an image screen. Each voxel is assigned a colour and partial opacity, which are both related to the radioactivity of the corresponding data point. An advantage of the volume rendering technique is that it allows inspection of the voxel matrix from various angles. It is thereby possible to visualise the distribution of radioligand binding.

The PET data frames corresponding to the time interval from 9 to 63 min after injection of the radioligand were summed into one 3D voxel matrix and used for volume rendering in the present study. This 3D voxel matrix consists of 147 planes of data with 256×256 pixels (1 mm$^3$ voxels) representing the presence of the radioligand binding in the brain. In the present study a high opacity was assigned to high and medium radioactivity voxels. The computer program VoxelView/Ultra 2.2 (Vital Images, Inc., USA) was used in this work [45].

## Results

### *Chemistry*

The incorporation of [$^{11}$C]methyl triflate to [$^{11}$C]PE2I was 80% using 0.5 mg of the acid precursor (Fig. 2). The total radiochemical yield of [$^{11}$C]PE2I, calculated from end of bombardment (EOB) and decay corrected, was 50% with a total synthesis time of 30–35 min.

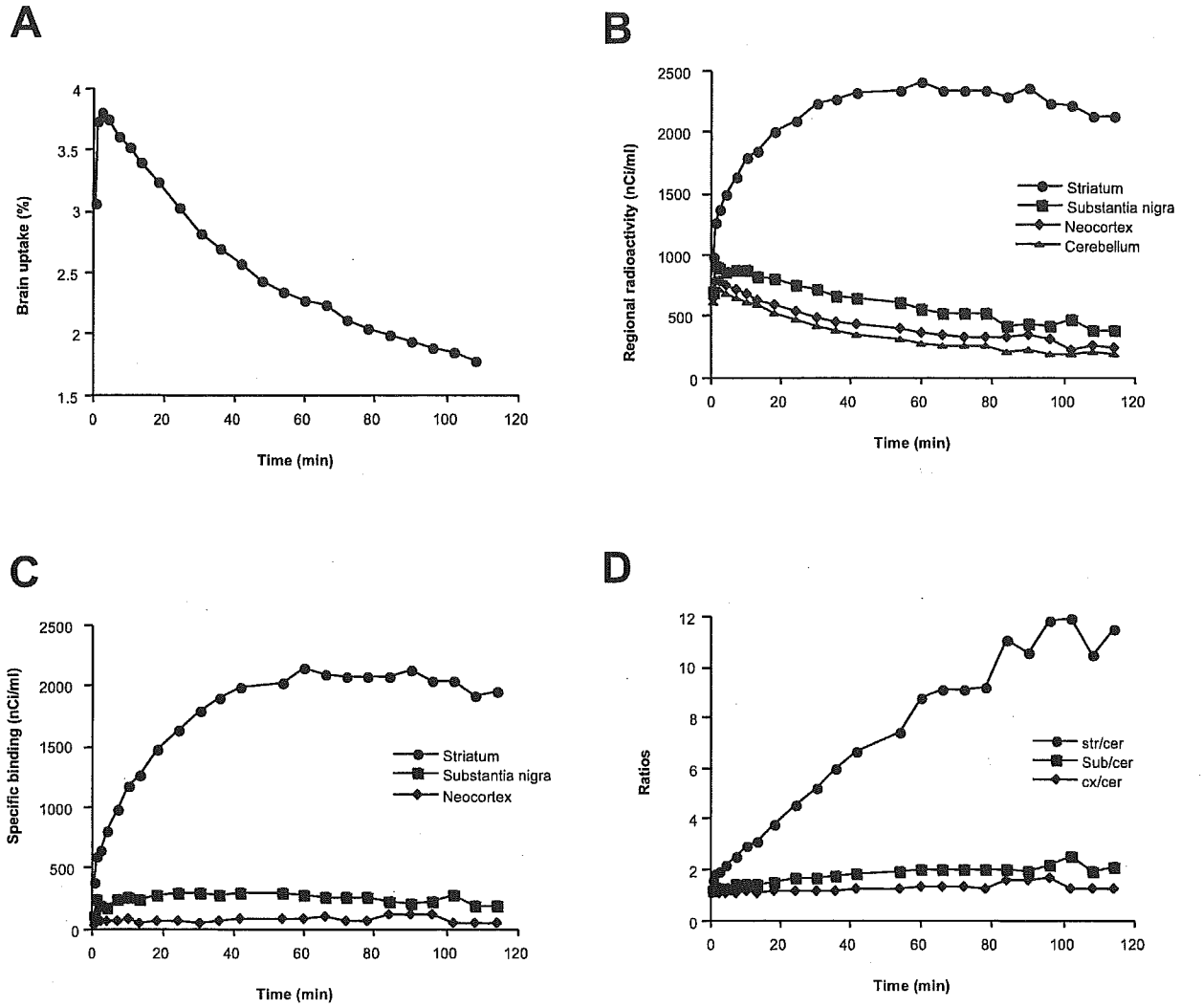


**Fig. 4.** **A** Total brain radioactivity uptake in the brain of a cynomolgus monkey after intravenous injection of [$^{11}$C]PE2I. **B** Time course for regional radioactivity (nCi/ml). **C** Specific binding (nCi/ml). **D** Binding ratio

Purification was performed by semi-preparative reversed phase HPLC (Fig. 3), yielding [$^{11}$C]PE2I with a radiochemical purity better than 99%. The retention times of [$^{11}$C]PE2I and free acid precursor were 7–9 and 2 min, respectively (Fig. 3). The retention time of [$^{11}$C]PE2I was 6 min on the analytical reversed-phase HPLC system. The specific radioactivity obtained at time of injection of [$^{11}$C]PE2I was about 1,500 Ci/mmol (55 GBq/μmol), corresponding to a total mass injected of about 0.3 μg in the studies in monkey and 1.5 μg in the human studies.

*PET measurements in monkeys*

At 4 min after i.v. injection of [$^{11}$C]PE2I in cynomolgus monkeys, 3.8% of the total radioactivity injected was present in brain (Fig. 4A). The uptake was highest in the striatum, lower in the substantia nigra and neocortex, and much lower in the cerebellum (Fig. 4B). The radioactivity ratios of the striatum and substantia nigra to the cerebellum increased continuously with time (Fig. 4D). The curve for specific binding in the striatum reached a peak level at about 60 min after injection (Fig. 4C).

The specificity of [$^{11}$C]PE2I binding was examined in displacement and pretreatment measurements. Following injection of β-CIT (0.5 mg/kg) at 20 min after injection of [$^{11}$C]PE2I, the radioactivity decreased rapidly and approached the curve for the cerebellum (Fig. 5A). In a pretreatment measurement where the selective dopamine transporter GBR 12909 (5 mg/kg) was given i.v. 8 min before the injection of [$^{11}$C]PE2I, the radioactivity was much lower than in the baseline measurements and close to the curve for the cerebellum. The reduction of specific [$^{11}$C]PE2I binding in the striatum, substantia nigra and

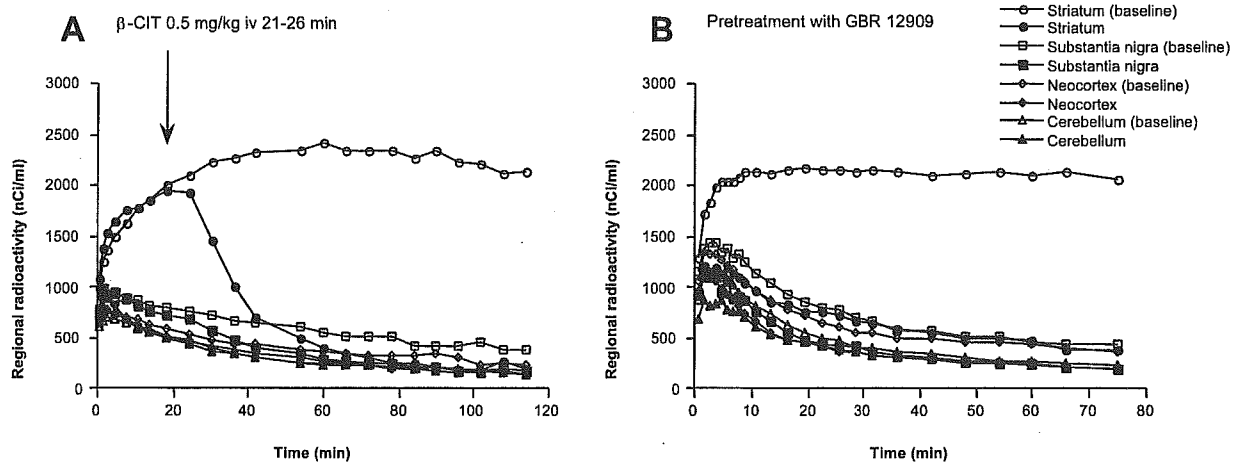


**Fig. 5A, B.** Time course for regional radioactivity (nCi/ml) in the brain of a cynomolgus monkey after intravenous injection of [$^{11}$C]PE2I. **A** Control and displacement experiments. **B** Control and pretreatment experiments. In the displacement experiment β-CIT (0.5 mg/kg) was given at 21–26 min, and in the pretreatment experiment GBR 12909 (5 mg/kg) was given 5 min before injection of [$^{11}$C]PE2I

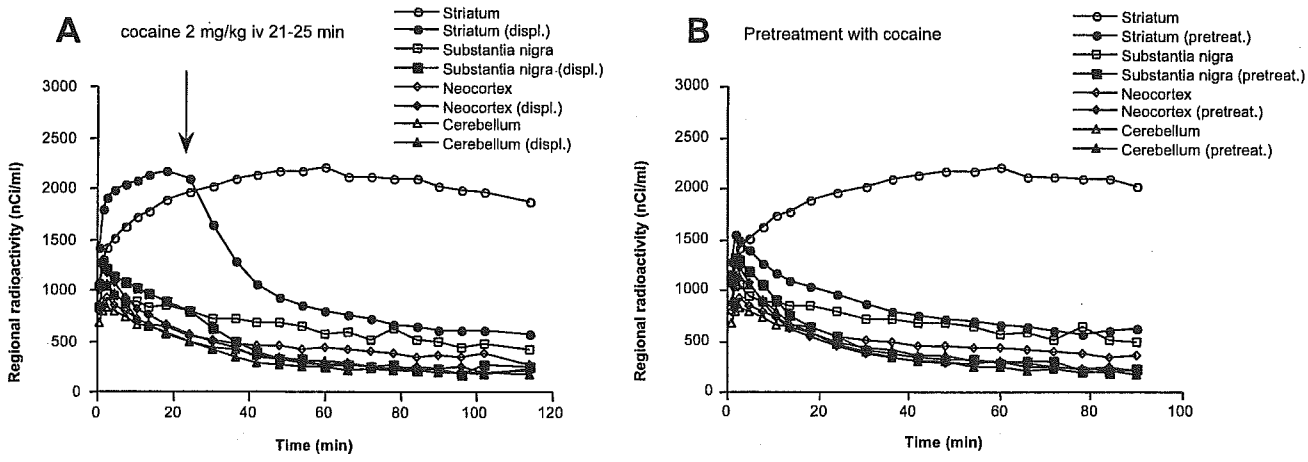


**Fig. 6A, B.** Time course for regional radioactivity (nCi/ml) in the brain of a cynomolgus monkey after intravenous injection of [$^{11}$C]PE2I. **A** Control and displacement experiments. **B** Control and pretreatment experiments. In the displacement experiment cocaine (2 mg/kg) was given at 21–25 min, and in the pretreatment experiment cocaine (2 mg/kg) was given 5 min before injection of [$^{11}$C]PE2I

the neocortex was about 80% at 40 min after injection (Fig. 5B).

Following injection of cocaine (2 mg/kg) in a displacement (Fig. 6A) and a pretreatment measurement (Fig. 6B), the striatal, thalamic and neocortical curves were markedly decreased and approached the curve for the cerebellum.

In pretreatment measurements where the selective noradrenaline transporter maprotiline (5 mg/kg) or the selective serotonin transporter citalopram (5 mg/kg) was injected i.v. 5 min before the injection of [$^{11}$C]PE2I, there was no evident effect on [$^{11}$C]PE2I binding (Fig. 7).

*PET measurement in human*

Initially there was a high transient peak of radioactivity in whole blood and plasma. Four minutes after injection of [$^{11}$C]PE2I, 8% of the radioactivity was present in the brain (Fig. 8A). The radioactivity in the striatum increased rapidly and reached a maximum level within 15 min (Figs. 8B and 9). Radioactivity ratios of the striatum and substantia nigra to the cerebellum were 10 and 1.8, respectively (Fig. 8D) at peak equilibrium, which was reached at about 40 and 20 min, respectively, after injection (Fig. 8C).

*Volume rendering*

The volume rendering technique was used to visualise the binding of [$^{11}$C]PE2I in the monkey brain, before and after displacement with β-CIT (Fig. 10, bottom). Binding in the striatum could be clearly visualised at baseline

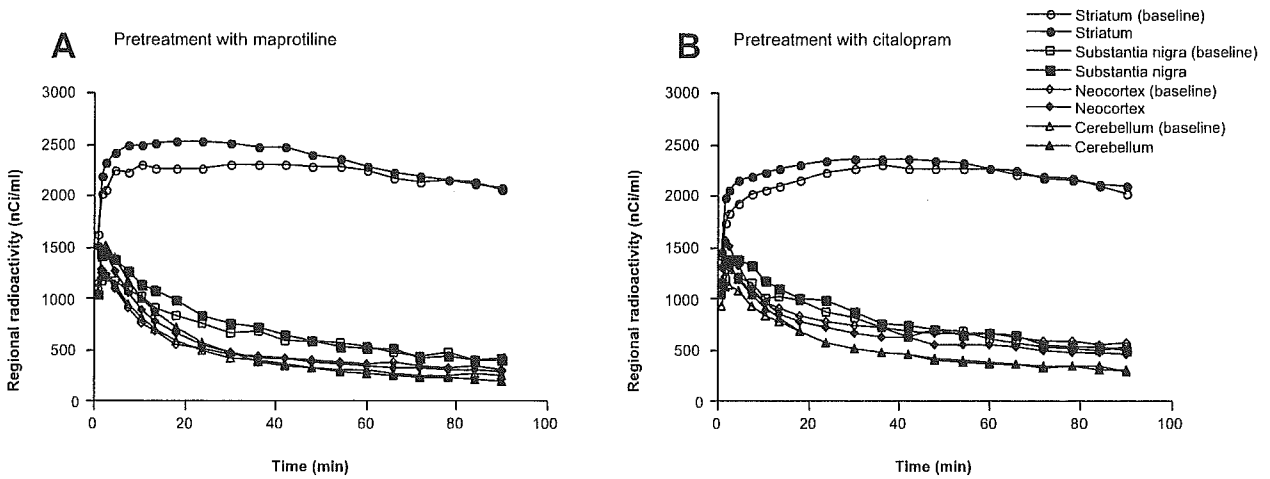


**Fig. 7A, B.** Time course for regional radioactivity (nCi/ml) in the brain of a cynomolgus monkey after intravenous injection of [$^{11}$C]PE2I. Control and pretreatment experiments. In one pretreatment experiment maprotiline (5 mg/kg) was given 5 min before injection of [$^{11}$C]PE2I (**A**). In a second pretreatment experiment citalopram (5 mg/kg) was given 5 min before injection of [$^{11}$C]PE2I (**B**)

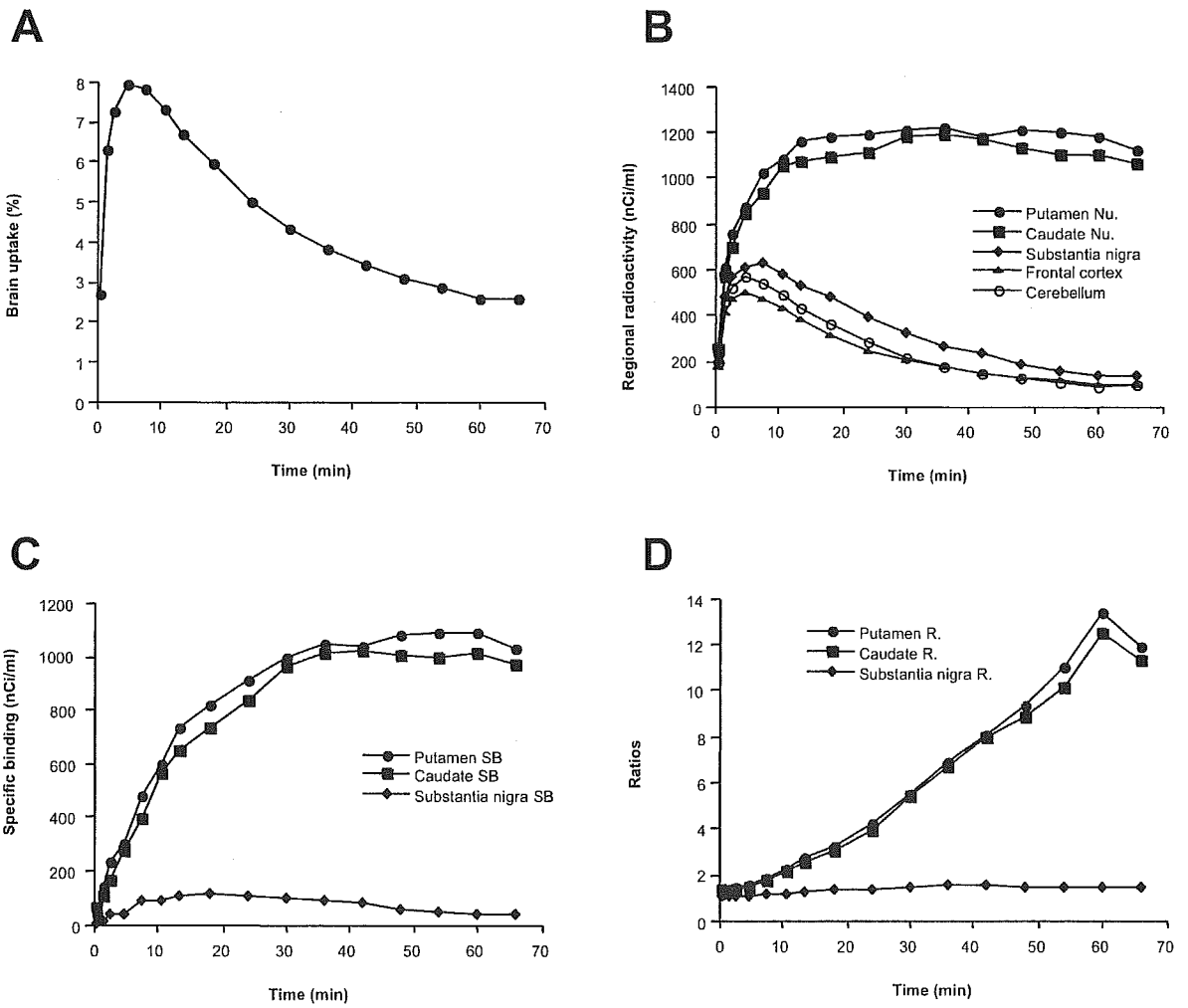


**Fig. 8.** **A** Total brain radioactivity uptake in the brain of a healthy human subject after intravenous injection of [$^{11}$C]PE2I. **B** Time course for regional radioactivity (nCi/ml). **C** Specific binding (nCi/ml). **D** Binding ratio

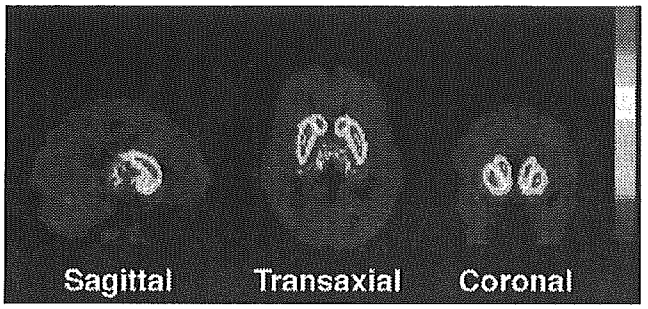


**Fig. 9.** Colour-coded PET image showing the distribution of radioactivity in the human brain after injection of about 293 MBq [$^{11}$C]PE2I (measured between 9 and 68 min)

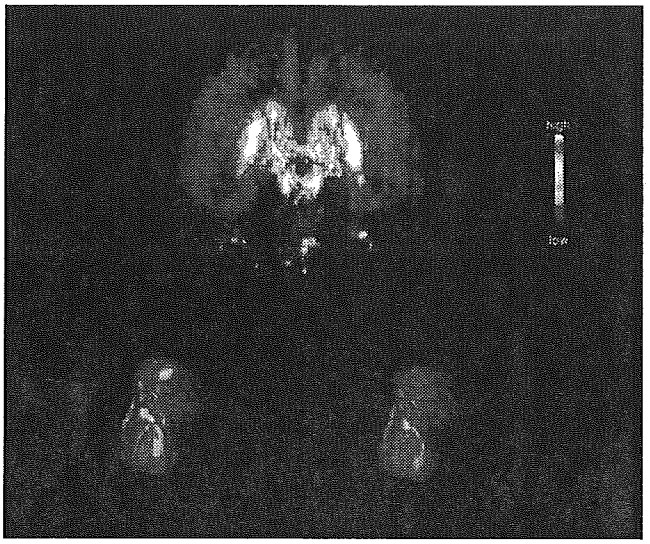

**Fig. 10.** Distribution of dopamine transporter [$^{11}$C]PE2I binding visualised by volume rendering of radioactive uptake in PET experiments. *Top:* radioactivity uptake of [$^{11}$C]PE2I in the human brain. The binding to the caudate and putamen structures are marked; binding to substantia nigra are also visible. *Bottom:* the binding of [$^{11}$C]PE2I in the monkey brain before (*left*) and after displacement with β-CIT (0.5 mg/kg given at 21–26 min) (*right*)

(bottom left). Radioactivity was low in the remaining parts of the brain, indicating low non-specific binding in extrastriatal regions. After displacement (bottom right), the monkey brain was almost devoid of visible binding, indicating low binding of the radioligand to the dopamine transporter sites. The volume rendering included the head, neck and upper thorax. There was some uptake in the thoracic structures. This uptake could not be displaced by β-CIT. Figure 10 (top) shows the distribution of radioactivity in the human brain. Binding in the caudate and putamen is clearly visible. [$^{11}$C]PE2I binding in the substantia nigra is also visible.

### *Plasma metabolite studies*

Blood samples were processed, and plasma was isolated and extracted. The peaks of radioactivity were integrated simultaneously by the PC and the chemical identity was determined by the simultaneous addition of a standard of PE2I. The integrated values obtained were in good agreement with the collected fractions measured in the well counter. The resolution between radioligand and labelled metabolites was sufficient. Specific experiments showed that >98% of the injected radioactivity was recovered from the column.

The percentage of total radioactivity in plasma representing unchanged [$^{11}$C]PE2I in both monkey and human was 15–20% at 40 min after injection. All labelled metabolites are more polar than the parent compound (Fig. 11).

## Discussion

### *Chemistry*

For PET imaging of the dopamine transporter, several radioligands such as [$^{11}$C]β-CIT-FP, [$^{11}$C]β-CIT-FE and

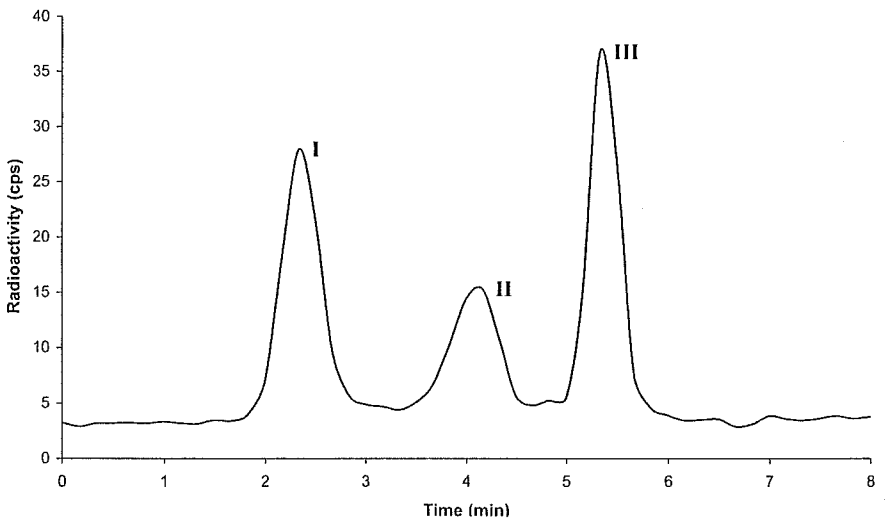


**Fig. 11.** Radiochromatogram from gradient HPLC analysis of human plasma, at 10 min after i.v. injection of [$^{11}$C]PE2I (peak III). Peaks I and II are more polar labelled metabolites

[$^{11}$C]β-CFT have previously been labelled with $^{11}$C by O- or N-methylation of the corresponding desmethyl compound with [$^{11}$C]methyl iodide [13, 18, 20]. The yield obtained after incorporation of [$^{11}$C]methyl iodide is usually sufficient for routine PET examinations. [$^{11}$C]Methyl triflate has recently been introduced as a more powerful methylating agent than [$^{11}$C]methyl iodide [31]. The use of [$^{11}$C]methyl triflate in the labelling of [$^{11}$C]PE2I resulted in higher yields, and no extra reaction time after trapping was needed, which is of importance for reliable routine production.

*PET measurements*

Four minutes after injection of [$^{11}$C]PE2I, 3.8% ($n$=5) of the total radioactivity injected was present in the monkey brain and 8% in the human brain. This uptake is higher than the total uptake of 1–2% previously demonstrated for useful PET radioligands such as [$^{11}$C]SCH 23390 and [$^{11}$C]raclopride [46, 47, 48] and provides a good signal for analysis of DAT binding.

The regional distribution of radioactivity was in accordance with the known distribution of DAT in vitro, with highest density in the basal ganglia, lower density in the substantia nigra and neocortex and much lower density in the cerebellum (Figs. 4, 8 and 9). The cerebellum is a region with a negligible density of DAT in vitro [27, 41]. The radioactivity in the cerebellum was therefore used as an estimate of the time curve for free and non-specifically bound radioligand concentration in brain. There was no effect of any of the compounds used in the displacement or pretreatment measurements on the ratio of radioactivity in the cerebellum to blood. This observation supports the use of the cerebellum as a reference region.

The specificity of [$^{11}$C]PE2I binding to DAT was demonstrated by displacement and pretreatment measurements with three reference compounds for DAT. The radioactivity in the striatum, substantia nigra and neocortex were markedly reduced after i.v. injection of β-CIT (0.5 mg/kg), GBR 12909 (5 mg/kg) or cocaine (2 mg/kg) (Figs. 5 and 6), indicating that a high proportion of [$^{11}$C]PE2I represents specific binding to DAT. Higher doses with the potential to completely displace [$^{11}$C]PE2I binding were not used owing to animal safety precautions.

The selectivity of [$^{11}$C]PE2I binding to DAT was examined in pretreatment measurements. There was no obvious effect on the regional time curve of the selective noradrenaline reuptake antagonist maprotiline (5 mg/kg) (Fig. 7A) or the selective serotonin reuptake antagonist citalopram (5 mg/kg) (Fig. 7B). These observations are consistent with the more extensive pharmacological characterisation performed previously in rodents in vitro, demonstrating that PE2I binds selectively to DAT [26, 27, 28]. The results of the present PET study indicate that [$^{11}$C]PE2I binds selectively to DAT in vivo, which is an advantage when compared with previously used tracers such as [$^{11}$C]β-CIT, [$^{11}$C]β-CIT-FE or [$^{11}$C]β-CIT-FP [14, 18, 20].

The density of the DAT is high in the striatum (>300 pmol/ml), much lower in the substantia nigra (about 50 pmol/ml) and almost negligible in other brain regions [27, 41]. The striatum to cerebellum ratio of about 10 in the monkey and human brain is higher than that previously reported for [$^{11}$C]β-CIT-FE, [$^{11}$C]β-CFT and other cocaine analogues [9, 20, 21]. The high ratio should be of advantage for subregional analysis of striatal [$^{11}$C]PE2I binding in neuropsychiatric brain disorders.

An interesting additional opportunity emerged from the 3D PET study of [$^{11}$C]PE2I binding in the human brain (Fig. 10). Using this highly selective radioligand, an evident signal was also obtained for the substantia nigra. The substantia nigra uptake of [$^{11}$C]PE2I is high when compared with previously developed PET tracers for DAT, with a ratio of 1.8 to cerebellum at peak equilibrium. Given the demonstrated selectivity of PE2I, the uptake in substantia nigra must be considered to be mainly binding to DAT.

In the human brain, high ratios were obtained for the striatum. This ratio is higher than the ratios previously obtained for [$^{11}$C]β-CIT-FE [20, 21]. Transient equilibrium was reached during the duration of a PET measurement (55–65 and 40–50 min, respectively). This time is earlier than that previously observed for [$^{11}$C]β-CFT and within the time of data acquisition for an $^{11}$C-labelled radioligand. The earlier peak of equilibrium and the binding selectivity indicate that [$^{11}$C]PE2I should be a suitable radioligand for quantitation of both striatal and substantia nigra binding of DAT.

*Plasma metabolite studies*

[$^{11}$C]PE2I was rather rapidly metabolised in monkey and human plasma (Fig. 11). Rapid metabolism is seen for many radioligands and does not preclude that [$^{11}$C]PE2I may be useful in PET studies. A problem may arise if the labelled metabolites pass the blood-brain barrier and bind to dopamine receptors. The labelled metabolites of [$^{11}$C C]PE2I observed by HPLC are all polar. It is thus unlikely that significant amounts of the major labelled metabolites might pass the blood-brain barrier.

*Conclusion*

[$^{11}$C]PE2I bound with high affinity, specificity and selectivity to central DAT as demonstrated by displacement experiments in the monkey brain in vivo. In the human subject, [$^{11}$C]PE2I reached a fast peak equilibrium and gave a high signal to noise ratio not only in the striatum

but also in the thalamic brain region. [$^{11}$C]PE2I should be suitable for quantitation of both striatal and substantia nigra DAT in man. This is particularly useful for research on neuropsychiatric and neurodegenerative diseases.

*Acknowledgements.* The authors would like to thank the members of the Stockholm PET group for their assistance in the PET experiments. Grants from the Swedish Medical Research Council (12983-01A), Karolinska Institutet, INSERM-MFR, the Région Centre (France) and European program (COST B12) supported this work. Nina Erixon-Lindroth was supported by the Swedish Foundation for Strategic Research.

## References

1. Malison RT, McDougle CJ, van Dyck CH, Scahill L, Baldwin RM, Seibyl JP, Price LH, Leckman JF, Innis RB. [$^{123}$I]beta-CIT SPECT imaging of striatal dopamine transporter binding in Tourette's disorder. *Am J Psychiatry* 1995; 152:1359–1361.
2. Malison RT, Best SE, van Dyck CH, McCance EF, Wallace EA, Laruelle M, Baldwin RM, Seibyl JP, Price LH, Kosten TR, Innis RB. Elevated striatal dopamine transporters during acute cocaine abstinence as measured by [$^{123}$I]beta-CIT SPECT. *Am J Psychiatry* 1998; 155:832–834.
3. Tissingh G, Bergmans P, Booij J, Winogrodzka A, van Royen EA, Stoof JC, Wolters EC. Drug-naive patients with Parkinson's disease in Hoen and Yahr stages I and II show a bilateral decrease in striatal dopamine transporters as revealed by [$^{123}$I]β-CIT SPECT. *J Neurol* 1998; 245:14–20.
4. Laasonen-Balk T, Kuikka J, Viinamaki H, Husso-Saastamoinen M, Lehtonen J, Tiihonen J. Striatal dopamine transporter density in major depression. *Psychopharmacology* 1999; 144: 282–285.
5. Dougherty DD, Bonab AA, Spencer TJ, Rauch SL, Madras BK, Fischman AJ. Dopamine transporter density in patients with attention deficit hyperactivity disorder. *Lancet* 1999; 354:2132–2133.
6. Krause KH, Dresel SH, Krause J, Kung HF, Tatsch K. Increased striatal dopamine transporter in adults patients with attention deficit hyperactivity disorder: effects of methylphenidate as measured by single photon emission computed tomography. *Neurosci Lett* 2000; 285:107–110.
7. Marek K, Innis RB, van Dyck CH, Fussell B, Early M, Eberly S, Oakes D, Seibyl JP. [$^{123}$I]beta-CIT SPECT imaging assessment of the rate of Parkinson's disease progression. *Neurology* 2001; 57:2089–2094.
8. Parkinson study group. Dopamine transporter brain imaging to assess the effects of pramipexole vs levedopa on Parkinson's disease progression. *JAMA* 2002; 287:1653–1667.
9. Halldin C, Gulyas B, Langer O, Farde L. Brain radioligands – state of the art and new trends. *Q J Nucl Med* 2001; 45:139–152.
10. Neumeyer JL, Wang S, Milius RA, Baldwin RM, Zea-Ponce Y, Hoffer PB, Sybirska E, Al-Tikriti M, Charney DS, Malison RT, Laruelle M, Innis RB. [$^{123}$I]-2β-carbomethoxy-3β-(4-iodophenyl)tropane: High-affinity SPECT radiotracer of monoamine reuptake sites in brain. *J Med Chem* 1991; 34:3144–3146.
11. Innis RB, Seibyl JP, Scanley BE, Laruelle M, Abi-Dargham A, Wallace E, Baldwin RM, Zea-Ponce Y, Zoghbi S, Wang S, Gao Y, Neumeyer JL, Charney DS, Hoffer PB, Marek KL. Single photon computed tomographic imaging demonstrates loss of striatal dopamine transporters on Parkinson disease. *Proc Natl Acad Sci USA* 1993; 90:11965–11969.
12. Müller L, Halldin C, Farde L, Karlsson P, Hall H, Swahn C-G, Neumeyer JL, Gao Y. Milius R. [$^{11}$C]β-CIT, a cocaine analogue preparation, autoradiography and preliminary PET investigations. *Nucl Med Biol* 1993; 20:249–255.
13. Någren K, Müller L, Halldin C, Swahn CG, Lehikoinen P. Improved synthesis of some commonly used PET radioligands by the use of [$^{11}$C]methyl triflate. *Nucl Med Biol* 1995; 22:235–239.
14. Farde L, Halldin C, Müller L, Suhara T, Karlsson P, Hall H. PET study of [$^{11}$C]β-CIT binding to monoamine transporters in the monkey and human brain. *Synapse* 1994; 16:93–103.
15. Neumeyer JL, Wang S, Gao Y, Milius RA, Kula NS, Campbell A, Baldessarini RJ, Zea-Ponce Y, Baldwin RM, Innis RB. *N*-ω-Fluoroalkyl analogs of (1*R*)-2β-carbomethoxy-3β-(iodophenyl)tropane (β-CIT): radiotracers for positron emission tomography and single photon emission computed tomography imaging of dopamine transporters. *J Med Chem* 1994; 37: 1558–1561.
16. Baldwin RM, Zea-Ponce Y, Al-Tikriti MS, Zoghbi SS, Seibyl JP, Charney DS, Hoffer PB,Wang S, Milius RA, Neumeyer JL, Innis RB. Regional brain uptake and pharmacokinetics of [$^{123}$I]N-ω-fluoroalkyl-2β-carboxy-3β-(4-iodophenyl)nortropane esters in baboons. *Nucl Med Biol* 1995; 22:211–219.
17. Kuikka JT, Bergström KA, Ahonen A, Hiltunen J, Haukka J, Länsimies E, Wang S. Neumeyer JL. Comparison of iodine-123 labeled 2β-carbomethoxy-3β-(4-iodophenyl)tropane (β-CIT) and 2β-carbomethoxy-3β-(4-iodophenyl)-*N*-(3-fluoropropyl)nortropane (β-CIT-FP) for the dopamine transporters in the living human brain. *Eur J Nucl Med* 1995; 22:682–686.
18. Lundkvist C, Halldin C, Ginovart N, Swahn C-G, Farde L. [$^{18}$F]β-CIT-FP is superior to [$^{11}$C]β-CIT-FP for quantitation of the dopamine transporter. *Nucl Med Biol* 1997; 24:621–627.
19. Chaly T, Dhawan V, Kazumata K, et al. Radiosynthesis of [$^{18}$F]*N*-3-fluoropropyl-2-β-carbomethoxy-3-β-(4-iodophenyl)nortropane and the first human study with positron emission tomography. *Nucl Med Biol* 1996; 23:999–1004.
20. Halldin C, Farde L, Lundkvist C, Ginovart N, Nakashima Y, Karlsson P, Swahn C-G. [$^{11}$C]β-CIT-FE, a radioligand for quantitation of dopamine transporters in the living brain using positron emission tomography. *Synapse* 1996; 22:386–390.
21. Farde L, Ginovart N, Halldin C, Chou Y-H, Olsson H, Swahn C-G. A PET study of [$^{11}$C]β-CIT-FE, binding to the dopamine transporter in the monkey and human brain. *Int J Neuropsychopharm* 2000; 3:203–214.
22. Günther I, Hall H, Halldin C, Swahn C-G, Farde L, Sedvall G. [$^{125}$C]β-CIT-FE and [$^{125}$C]β-CIT-FP are superior to [$^{125}$C]β-CIT for dopamine transporter visualisation: autoradiographic evaluation in the human brain. *Nucl Med Biol* 1997; 24:629–634.
23. Wong DF, Yung B, Dannals RF, Shaya EK, Ravert HT, Chen CA, Chan B, Folio T, Scheffel U, Ricaurte GA, Neumeyer JL, Wagner HN, Kuhar MJ. In vivo imaging of baboon and human dopamine transporters by positron emission tomography using [$^{11}$C]WIN 35,428. *Synapse* 1993; 15:130–142.
24. Laakso A, Bergman J, Haaparanta M, Vilkman H, Solin O, Hietala J. [$^{18}$F]CFT [($^{18}$F)WIN 35,428], a radioligand to study the dopamine transporter with PET: characterization in human subjects. *Synapse* 1998; 28:244–250.
25. Fischman AJ, Bonab AA, Babich JW, Palmer EP, Alpert NM, Elmaleh DR, Callahan RJ, Barrow SA, Graham W, Meltzer

PC, Hanson RN, Madras BK. Rapid detection of Parkinson's disease by SPECT with altropane: a selective ligand for dopamine transporters. *Synapse* 1998; 29:128–141.

26. Chalon S, Garreau L, Emond P, Zimmer L, Vilar MP, Besnard J-C, Guilloteau D. Pharmacological characterization of *(E)-N*-(3-iodoprop-2-enyl)-2β-carbomethoxy-3β-(4′-methylphenyl)nortropane as a selective and potent inhibitor of the neuronal dopamine transporter. *J Pharmacol Exp* 1999; 291:648–654.
27. Hall H, Halldin C, Guilloteau D, Besnard J-C, Emond P, Chalon S, Farde L, Sedvall G. Specific visualization of the dopamine transporter in the human brain post-mortem with the new selective ligand [$^{125}$I]PE2I. *Neuroimage* 1999; 9:108–116.
28. Emond P, Garreau L, Chalon S, Boazi M, Caillet M, Bricard J, Frangin Y, Mauclaire L, Besnard J-C, Guilloteau D. Synthesis and ligand binding of nortropane derivatives: N-substituted-2β-carbomethoxy-3β-(4′-iodophenyl)nortropane and *N*-(3-iodoprop-2*E*-enyl)-2β-carbomethoxy-3β-(3′,4′-disubstituted phenyl)nortropane. New affinity and selectivity compounds for the dopamine transporter. *J Med Chem* 1997; 40:1366–1372.
29. Guilloteau D, Emond P, Baulieu JL, Garreau L, Frangin Y, Pourcelot L, Mauclaire L, Besnard J-C, Chalon S. Exploration of the dopamine transporter: in vitro and in vivo characterization of a high-affinity and high-specificity iodinated tropane derivative (*E*)-*N*-(3-iodoprop-2-enyl)-2β-carbomethoxy-3β-(4′-methylphenyl)nor-tropane (PE2I). *Nucl Med Biol* 1998; 25:331–337.
30. Kuikka JK, Baulieu JL, Hiltunen J, Halldin C, Bergström K, Farde L, Emond P, Chalon S, Yu M, Nikula T, Laitinen T, Karhu J, Tupala E, Hallikainen T, Kolehmainen V, Mauclaire L, Maziere B, Tiihonen J, Guilloteau D. Pharmacokinetics and dosimetry of iodine-123 labelled PE2I in humans, a radioligand for dopamine transporter imaging. *Eur J Nucl Med* 1998; 25:531–534.
31. Jewett DM. A simple synthesis of [$^{11}$C]methyl triflate. *Appl Radiat Isot* 1992; 43:1383–1385.
32. Sandell J, Langer O, Larsen P, Dolle F, Vaufrey F, Demphel S, Crouzel C, Halldin C. Improved specific radioactivity of the PET radioligand [$^{11}$C]FLB457 by the use of GE Medical Systems PETtrace MeI Microlab. *J Lab Compd Radiopharm* 2000; 43:331–338.
33. Wienhard K, Dahlbom M, Eriksson L, Michel C, Bruckbauer T, Pietrzyk U, Heiss W-D. The ECAT EXACT HR: performance of a new high resolution positron scanner. *J Comput Assist Tomogr* 1994; 18:110–118.
34. Karlsson P, Farde L, Halldin C, Swahn C-G, Sedvall G, Foged C, Hansen KT, Skrumsager B. PET examination of [$^{11}$C]NNC 687 and [$^{11}$C]NNC 756 as new radioligands for the D1-dopamine receptor. *Psychopharmacology* 1993; 113:149–156.
35. Andersen P. The dopamine uptake inhibitor GBR12909: selectivity and molecular mechanisms of action. *Eur J Pharmacol* 1989; 166:493–504.
36. Pinder R, Brogden R, Speight T, Avery G. Maprotiline: a review of its pharmacological properties and therapeutic efficacy in mental depressive states. *Drugs* 1977; 13:321–352.
37. Hyttel J. Citalopram: Pharmacological profile of a specific serotonin uptake inhibitor with antidepressant activity. *Prog Neuropsychopharmacol Biol Psychiatry* 1982; 6:277–295.
38. Bergström M, Boëthius J, Eriksson L, Greitz T, Ribbe T, Widén L. Head fixation device for reproducible position alignment in transmission CT and positron emission tomography. *J Comput Assist Tomogr* 1981; 5:136–141.
39. Eriksson L, Holte S, Bohm C, Kesselberg M, Hovander B. Automated blood sampling system for positron emission tomography. *IEEE Trans Nucl Sci* 1988; 35:703–707.
40. Halldin C, Swahn C-G, Farde L, Sedvall G. Radioligand disposition and metabolism. Key information in early drug development. In: Comar D, ed. *PET for drug development and evaluation*. Dordrecht: Kluwer Academic; 1995:55–65.
41. Madras BK, Gracz LM, Meltzer PC, Liang AY, Elmaleh DR, Kaufman MJ, Fischman AJ. Altropane, a SPECT or PET imaging probe for dopamine neurons. II. Distribution to dopamine-rich regions of primate brain. *Synapse* 1998; 29:105–115.
42. Farde L, Eriksson L, Blomqvist G, Halldin C. Kinetic analysis of central [$^{11}$C]raclopride binding to D2-dopamine receptors studied by PET—a comparison to the saturation analysis. *J Cerebr Blood Flow Metab* 1989; 9:696–708.
43. Ito H, Hietala J, Blomqvist G, Halldin C, Farde L. Comparison of the transient equilibrium and continous infusion method for quantitative PET analysis of [$^{11}$C]raclopride binding. *J Cereb Blood Flow Metab* 1998; 18:941–950.
44. Drebin RA, Carpenter L, Hanrahan P. Volume rendering. *Comput Graph* 1988; 22:65–74.
45. Pauli S, Sedvall G. Three-dimensional visualization of the benzodiazepine receptor population within a living human brain using PET and MRI. *Eur Arch Psychiatry Clin Neurosci* 1997; 247:61–70.
46. Farde L, Halldin C, Stone-Elander S, Sedvall G. Analysis of human dopamine receptor subtypes using $^{11}$C-SCH 23390 and $^{11}$C-raclopride. *Psychopharmacology* 1987; 92:278–284.
47. Halldin C, Farde L, Högberg T, Hall H, Ström P, Ohlberger A, Solin O. A comparative PET-study of five carbon-11 or fluorine-18 labelled salicylamides. Preparation and in vitro dopamine D-2 binding. *Nucl Med Biol* 1991; 18:871–881.
48. Farde L, Pauli S, Hall H, Eriksson L, Halldin C, Högberg T, Nilsson L, Sjögren I, Stone-Elander S. Stereoselective binding of $^{11}$C-raclopride in living human brain—a search for extrastriatal central D2-dopamine receptors by PET. *Psychopharmacology* 1988; 94:471–478.

*Journal of Cerebral Blood Flow & Metabolism*
23:1096–1112 © 2003 The International Society for Cerebral Blood Flow and Metabolism
Published by Lippincott Williams & Wilkins, Inc., Baltimore

# Linearized Reference Tissue Parametric Imaging Methods: Application to [$^{11}$C]DASB Positron Emission Tomography Studies of the Serotonin Transporter in Human Brain

*Masanori Ichise, *Jeih-San Liow, *Jian-Qiang Lu, †Akihiro Takano, *Kendra Model, *Hiroshi Toyama, †Tetsuya Suhara, †Kazutoshi Suzuki, *Robert B. Innis, and ‡Richard E. Carson

**Molecular Imaging Branch, National Institute of Mental Health, †Brain Imaging Project, National Institute of Radiological Sciences, Chiba, Japan, and ‡PET Department, Warren G. Magnuson Clinical Center, National Institutes of Health, Bethesda, Maryland, U.S.A.*

**Summary:** The authors developed and applied two new linearized reference tissue models for parametric images of binding potential (*BP*) and relative delivery ($R_1$) for [$^{11}$C]DASB positron emission tomography imaging of serotonin transporters in human brain. The original multilinear reference tissue model ($MRTM_O$) was modified (MRTM) and used to estimate a clearance rate ($k_2'$) from the cerebellum (reference). Then, the number of parameters was reduced from three (MRTM) to two (MRTM2) by fixing $k_2'$. The resulting *BP* and $R_1$ estimates were compared with the corresponding nonlinear reference tissue models, SRTM and SRTM2, and one-tissue kinetic analysis (1TKA), for simulated and actual [$^{11}$C]DASB data. MRTM gave $k_2'$ estimates with little bias (<1%) and small variability (<6%). MRTM2 was effectively identical to SRTM2 and 1TKA, reducing *BP* bias markedly over $MRTM_O$ from 12–70% to 1–4% at the expense of somewhat increased variability. MRTM2 substantially reduced *BP* variability by a factor of two or three over MRTM or SRTM. MRTM2, SRTM2, and 1TKA had $R_1$ bias <0.3% and variability at least a factor of two lower than MRTM or SRTM. MRTM2 allowed rapid generation of parametric images with the noise reductions consistent with the simulations. Rapid parametric imaging by MRTM2 should be a useful method for human [$^{11}$C]DASB positron emission tomography studies. **Key Words:** Positron emission tomography—Parametric imaging—Linearized reference tissue model—Noise-induced bias—Serotonin transporters—[$^{11}$C]DASB.

The central serotonergic (5-HT) system has been linked to the pathophysiology and drug treatment of neuropsychiatric conditions such as depression and obsessive compulsive disorder (Lopez-Ibor, 1988). The serotonin transporter (SERT) is a critical modulator of 5-HT neurotransmission and the site of action of commonly used antidepressant drugs (Lesch, 1997). Therefore, *in vivo* imaging of the SERT has been of intense interest as a tool to study 5-HT function in health and disease. A recently developed highly selective radioligand, [$^{11}$C]-3-amino-4-(2-dimethylaminomethyl-phenylsulfanyl)-benzonitrile ([$^{11}$C]DASB), is most promising for positron emission tomography (PET) imaging of SERT in human brain (Ginovart et al., 2001; Houle et al., 2000; Huang et al., 2002; Wilson et al., 2000a). [$^{11}$C]DASB binds reversibly to SERT with high affinity and selectivity (Wilson et al., 2000a, 2002), and displays moderately high specific-to-nonspecific ratios *in vivo* (Ginovart et al., 2001; Houle et al., 2000). [$^{11}$C]DASB tissue data can be described by a one-tissue (1T) compartment model (Ginovart et al., 2001) and SERT binding potential (*BP*; Mintun et al., 1984) can be estimated using the cerebellum, which contains few SERT binding sites, as reference tissue instead of an arterial input function. The regional distribution of *BP* correlates well with SERT densities in human brain (Ginovart et al., 2001; Houle et al., 2000).

Reference tissue methods have been widely used to estimate neuroreceptor *BP* because these methods

Received February 14, 2003; final version received June 12, 2003; accepted June 16, 2003.

Supported by the Neuroscience project of the National Institute of Radiological Sciences, Chiba, Japan, and Japan Society for the Promotion of Science, Grant-in-Aid for Scientific Research 14370296, Tokyo, Japan.

Address correspondence and reprint requests to Dr. Ichise, Building 1 B3–10, One Center Drive MSC0135, Molecular Imaging Branch, National Institute of Mental Health, Bethesda, MD 20892, U.S.A.; e-mail: masanori.ichise@nih.gov



DOI: 10.1097/01.WCB.0000085441.37552.CA

eliminate the invasive and often logistically difficult procedure of obtaining arterial input functions corrected for metabolites. For [$^{11}$C]DASB, reference tissue methods that yield parametric images of *BP* would be a valuable data analysis approach because SERT binding sites are widely distributed in the brain, including small limbic structures such as the raphe, hippocampus, and amygdala (Backstrom et al., 1989; Cortes et al, 1988; Rosel et al., 1997).

For reversibly binding neuroreceptor radioligands, several reference tissue models have been developed to estimate *BP* (Ichise et al., 1996; Lammertsma et al., 1996; Lammertsma and Hume, 1996; Logan et al., 1996) as well as a measure of radioligand delivery to tissue relative to reference region ($R_1$) (Lammertsma et al., 1996; Lammertsma and Hume, 1996). These models are generally an extension of either traditional compartmental kinetic models (Lammertsma et al., 1996; Lammertsma and Hume, 1996) or their linearized versions (Ichise et al., 1996; Logan et al., 1996). The computationally rapid linear least squares (LS) estimation algorithms used in the latter approach is well suited for rapid parametric imaging compared with the more computationally time-consuming nonlinear least squares (NLS) algorithms used in the former, although basis function methods can be used to improve NLS processing speed (Gunn et al., 1997). One drawback of the linear LS approach as originally described, however, is that statistical noise, particularly at the voxel level in the PET data, can introduce significantly bias in the parameter estimates (Carson, 1993; Slifstein and Laruelle, 2000). Subsequently, several strategies have been proposed to reduce noise-induced bias for LS parameter estimation (Carson, 1993; Ichise et al., 2002; Logan et al., 2001; Varga et al., 2002).

Here, we developed two new linearized reference tissue models that are resistant to noise, computationally fast, and do not require invasive blood sampling. These models were used to generate parametric images of *BP* and $R_1$ for [$^{11}$C]DASB PET data. To reduce noise effects, we applied two strategies to the multilinear reference tissue model (Ichise et al., 1996). First, the multilinear operational equation, which estimates three parameters including *BP* and $k_2'$ (the clearance rate constant from the reference region), was rearranged to remove a noisy tissue radioactivity term, $C(T)$, from the independent variables, following the strategy known to be effective in reducing the noise-induced bias for the LS models requiring blood data (Carson, 1993; Ichise et al., 2002). Second, the number of parameters in this newly rearranged multilinear reference tissue model (MRTM) was reduced from three to two, by fixing $k_2'$ to a value estimated by preliminary application of MRTM for selected regions of interest (ROIs), following the strategy also known to be effective in noise reduction for the NLS simplified reference tissue model (SRTM) (Wu and Carson, 2002). The parameter estimation results for this new two-parameter model (MRTM2) from simulated and actual [$^{11}$C]DASB data were compared with the other estimation methods, particularly the two-parameter SRTM (SRTM2) and the one-tissue kinetic analysis (1TKA) that requires blood data, with the hypothesis that MRTM2 will produce results comparable with SRTM2 and 1TKA If this is the case, then MRTM2 should be a highly useful data analysis tool for [$^{11}$C]DASB because parametric imaging with MRTM2 can be performed in a fraction of the computational time required for SRTM2 or 1TKA.

## MATERIALS AND METHODS

### Theory

**Multilinear reference tissue models.** The operational equation for the original multilinear reference tissue model ($MRTM_O$, Ichise et al., 1996) is as follows:

$$\frac{\int_0^T C(t)dt}{C(T)} = \frac{V}{V'}\frac{\int_0^T C'(t)dt}{C(T)} + \frac{V}{V'k_2'}\frac{C'(T)}{C(T)} + b \qquad (1)$$

where $C(t)$ and $C'(t)$ are the regional or voxel time–radioactivity concentrations in the tissue and reference regions, respectively (kBq/mL), $V$ and $V'$ are the corresponding total distribution volumes (mL/mL); $k_2'$ (min$^{-1}$) is the clearance rate constant from the reference region to plasma, and $b$ is the intercept term, which becomes constant for $T > t^*$. Eq. 1 allows estimation of three parameters, $\beta_1 = V/V'$, $\beta_2 = V/(V'k_2')$, and $\beta_3 = b$ by multilinear regression analysis for $T > t^*$. Note that Eq. 1 and all subsequent linear equations are applicable to both 1T and two-tissue (2T) compartment models. Assuming that the nondisplaceable distribution volumes in the tissue and reference regions are identical, *BP* ($BP = V/V' - 1$) is calculated from the first regression coefficient as $BP = (\beta_1 - 1)$. For radioligands with 1T kinetics such as [$^{11}$C]DASB (Ginovart et al., 2001), Eq. 1 is linear from $T = 0$, i.e., $t^* = 0$, and $b$ is equal to $(-1/k_2)$, where $k_2$ (min$^{-1}$) is the clearance rate constant from the tissue to plasma. For the 1T model, $V = K_1/k_2$ and $V' = K_1'/k_2'$, where $K_1$ and $K_1'$ (mL/min$^{-1}$/mL$^{-1}$) are the rate constants for transfer from plasma to the tissue and reference region, respectively, and $R_1 = K_1/K_1'$, the relative radioligand delivery, can be calculated from the ratio of the second and third regression coefficients as $R_1 = -\beta_2/\beta_3$.

Ordinary LS parameter estimation assumes that independent variables are noise-free. However, Eq. 1 contains a noisy term, $C(T)$, on the right-hand side (independent variables). In addition, the structure of Eq. 1 makes noise in the dependent (left-hand side) and independent variables correlated. These factors produce biased estimates (Carson, 1993; Ichise et al., 2002; Slifstein and Laruelle, 2000). Following the strategy described previously to reduce noise-induced bias for linear estimation of $V$ using tissue and blood data (Ichise et al., 2002), Eq. 1 can be rearranged to yield the following multilinear reference tissue model (MRTM):

$$C(T) = -\frac{V}{V'b}\int_0^T C'(t)dt + \frac{1}{b}\int_0^T C(t)dt - \frac{V}{V'k_2'b}C'(T) \qquad (2)$$

In Eq. 2, noisy $C(T)$ is no longer present in the independent variables, although integral of $C(t)$ is present. However, integrals of noisy data typically have much lower percent variation than the data themselves (Ichise et al., 2002). Additionally, the correlation of the noise in the dependent and independent variable is dramatically reduced in Eq. 2 compared with Eq. 1. Eq. 2 also allows estimation of three parameters, $\gamma_1 = -V/(V'b)$, $\gamma_2 = 1/b$ and $\gamma_3 = -V/(V'k_2'b)$, assuming that the integrals of $C(t)$ and $C'(t)$, as well as $C'(T)$, are noise-free. $BP$ can then be calculated from the ratio of the two regression coefficients as $BP = -(\gamma_1/\gamma_2 + 1)$. For the 1T model $R_1 = \gamma_3$ and $k_2 = -\gamma_2$.

Eq. 2 also allows estimation of $k_2'$, which is given by $k_2' = \gamma_1/\gamma_3$. However, a different value of $k_2'$ is estimated by Eq. 2 for each voxel, although there is only one reference region and therefore only one true value for $k_2'$. By fixing $k_2'$ to a value obtained with a preliminary analysis using Eq. 2, a two-parameter version of Eq. 2 (MRTM2) is obtained by rearrangement to yield

$$C(T) = -\frac{V}{V'b}\left(\int_0^T C'(t)dt + \frac{1}{k_2'}C'(T)\right) + \frac{1}{b}\int_0^T C(t)dt \quad (3)$$

Eq. 3 can also be obtained by rearrangement of the graphical reference tissue model described by Logan et al. (1996). Eq. 3 estimates two parameters, $\gamma_1 = -V/(V'b)$ and $\gamma_2 = 1/b$ for $T > t^*$, assuming that the integrals of $C(t)$ and $C'(t)$, as well as $C'(T)$, are noise-free. $BP$ is then calculated from the ratio of the two regression coefficients as $BP = -(\gamma_1/\gamma_2 + 1)$. For the 1T model, $R_1 = \gamma_1/k_2'$ and $k_2 = -\gamma_2$. Because MRTM2 estimates fewer parameters, it is expected to be more stable than MRTM, particularly at high-noise levels of voxel-based parametric imaging. This strategy has been shown to be effective in reducing noise from the three-parameter simplified reference tissue model (SRTM) to the two-parameter model SRTM2 (Wu and Carson, 2002).

## Simplified reference tissue models

The operational equation for the SRTM (Lammertsma and Hume, 1996) is

$$C(t) = R_1C'(t) + R_1(k_2' - k_2)C'(t) \otimes e^{-k_2't} \quad (4)$$

where $\otimes$ is the convolution symbol. Note that Eq. 4 is derived from the 1T compartment model unlike the above linear equations that are applicable to both 1T and 2T compartment models. Eq. 4 allows NLS estimation of three parameters from the entire data set, $R_1$, $k_2'$, and $k_2$. $BP$ is calculated from the relationship, $BP = R_1(k_2'/k_2) - 1$. In the two-parameter SRTM2 method (Wu and Carson, 2002), the value of $k_2'$ is fixed so that Eq. 4 estimates two parameters, $R_1$ and $k_2$.

**One-tissue compartment kinetic analysis.** The operational equation for 1TKA is

$$C(t) = K_1C_P(t) \otimes e^{-k_2t} \quad (5)$$

where $C_P(t)$ is the metabolite-corrected plasma concentration (kBq/mL). Eq. 5 allows NLS estimation of two parameters from the entire data set, $K_1$ and $k_2$. $BP$ and $R_1$ are calculated from the relationship, $BP = (K_1k_2'/K_1'k_2) - 1$ and $R_1 = K_1/K_1'$, where $K_1'$ and $k_2'$ are estimated by 1TKA applied to the reference region time–activity curve (TAC), with the following equation:

$$C'(t) = K_1'C_P(t) \otimes e^{-k_2't} \quad (6)$$

## Positron emission tomography studies

[$^{11}$C]DASB PET studies were performed in eight normal control subjects (mean age, 21.8 ± 2.4 years; age range, 20–27 years). The study protocol was approved by the ethics and radiation safety committees of the National Institute of Radiological Sciences (Chiba, Japan), and written informed consent was obtained from each subject. [$^{11}$C]DASB was synthesized as described previously (Wilson et al., 2000a,b). After a 10-minute transmission scan using a $^{68}$Ge-$^{68}$Ga source, dynamic PET scans were acquired for 90 minutes (27 frames consisting of 4 × 1, 13 × 2, 5 × 4 and 5 × 8-minute frames) after bolus administration of 630 ± 51 MBq (specific activity, 70–196 GBq/μmol at the time of injection) of [$^{11}$C]DASB on the ECAT 47 (CTI-Siemens, Knoxville, TN, U.S.A.) scanner in two-dimensional mode, which provides 47 slices with 3.38-mm center-to-center slice separation. To minimize head movement during each scan, head fixation devices (Fixster Instruments, Stockholm, Sweden) and thermoplastic attachments made to fit the individual subject were used. The PET data were reconstructed using a Hann filter with a cut-off frequency of 0.5 resulting in image full width at half maximum of 9.3 mm.

Arterial blood samples were taken 13 times during the initial 3 minutes after the tracer injection, then eight times during the next 17 minutes, and then once every 10 minutes until the end of the scan. Each blood sample was separated into plasma and blood cell fraction by centrifugation. For the plasma fractions at 3.5, 9, 19, 29, 39, 49, 59, 69, 79, and 89 minutes after injection, acetonitrile was added and the sample was centrifuged. The obtained supernatant was subjected to radio-HPLC analysis (column μBondapak C18; mobile phase, phosphoric acid [6 mmol/L]/$CH_3CN$ = 1:1; flow rate, 2.5 mL/min). The fraction of unchanged radioligand in plasma was fitted to a sum of two exponentials. A metabolite-corrected plasma curve was generated by the product of the plasma activity and metabolite fraction curves. The portion of the metabolite-corrected plasma curve beyond the initial peak was fit to a sum of two exponentials (three exponentials did not improve fitting). The resulting curve was used as the input function for estimation of 1T kinetic parameter values (see below). Plasma protein binding was not determined in the present study.

## Simulation analysis

Table 1 lists the characteristics of the six models used for the simulation analysis and the analysis of human PET data. For the simulation, bias and variability of $BP$ and $R_1$ estimates by all six models due to statistical noise were evaluated with simulated [$^{11}$C]DASB TACs at different noise levels. Gray matter regions with a range of $BP$ (raphe, striatum, thalamus, and frontal cortex) were simulated. Even though $BP$ measurement in white matter may not be of biological interest, simulations in white matter with very low $BP$ were also performed because poor estimation characteristics there would contribute to artifacts in parametric images.

In addition, the feasibility of obtaining a stable $k_2'$ value to be used for MRTM2 and SRTM2 was evaluated by application of MRTM to ROI TACs. To this end, bias and variability of $k_2'$ estimates by MRTM were calculated for simulated [$^{11}$C]DASB TACs at different ROI noise levels. The variability of $BP$ and $R_1$ estimates from simulation were, when appropriate, compared with the respective theoretical variability, as predicted by the Cramer-Rao (C-R) lower bounds for the two-parameter and three-parameter models (Beck and Arnold, 1977; Wu and Carson, 2002).

To perform [$^{11}$C]DASB TAC simulations, a metabolite-corrected plasma input function that had a typical clearance (175 L/h) was selected from a normal control study, and was

**TABLE 1.** *Model summary*

| | $MRTM_O$ | MRTM | SRTM | MRTM2 | SRTM2 | 1TKA |
|---|---|---|---|---|---|---|
| Model name | Original mutilinear reference tissue model | Multilinear reference tissue model | Simplified reference tissue model | Multilinear reference tissue model 2 | Simplified reference tissue model 2 | One-tissue-compartment kinetic analysis |
| Reference | Ichise et al. (1996) | Present work | Lammertsma and Hume (1996) | Present work | Wu and Carson (2002) | |
| Operational equation | Eq. 1 $C(t)$ in the denominator | Eq. 2 $C(t)$ moved to left side | Eq. 4 Convolution | Eq. 3 $C(t)$ moved to left side | Eq. 4 Convolution | Eq. 5 Convolution |
| No. of parameters | 3 | 3 | 3 | 2 | 2 | 2 |
| Fitting | Multilinear | Multilinear | Nonlinear | Multilinear | Nonlinear | Nonlinear |
| Input | Reference tissue | Reference tissue | Reference tissue | Reference tissue | Reference tissue | Plasma |
| $k_2'$ | Variable | Variable | Variable | Fixed | Fixed | Estimated from reference region fit (Eq. 6) |

scaled to a group mean injection dose of 630 MBq. TACs were simulated using the 1T parameter values (Table 2). Intravascular radioactivity was not included because its contribution would be minimal owing to the high $K_1$ and $V$ values. These parameter values were derived from the group mean $K_1'$, $K_1$, $V'$, and $V$ values estimated by 1T KA for the respective regions (see below).

Noise-free TACs were generated for 90 minutes (54 frames of 30-second to 4-minute duration with TAC values calculated at the midframe time). The sampling rates used in the simulations were twice the rates used in actual PET studies to minimize any bias introduced by the integral(s) on the right-hand side of the operational equations. Then, random amounts of normally distributed mean zero noise were added to the noise-free TAC with SD according to the following formula:

$$SD(t_i) = SF\left(\frac{e^{\lambda t_i}C(t_i)}{\Delta t_i}\right)^{0.5} \quad (7)$$

where $SF$ is the scale factor that controls the level of noise; $C(t_i)$ is the noise-free simulated radioactivity; $\Delta t_i$ is the scan duration (seconds); and $\lambda$ is the radioisotope decay constant. This model is appropriate in the case of low or constant randoms fractions, constant scatter fraction, and relatively unchanging emission distribution over time. One thousand noisy TACs were generated for several values of $SF$ so that TAC noise levels ranged from 5 to 30%. Percent TAC noise was calculated from the mean SD (Eq. 7) of the latter portion of the TAC (50 to 90 minutes). These noise levels would cover a range of TAC noise between that found in a small ROI to that of a voxel.

The noise-free reference tissue TAC for all reference tissue models and the true $k_2'$ value of 0.056 $min^{-1}$ for MRTM2 and SRTM2 were used in fitting noisy tissue TACs (see Discussion). Equal data weights were used for all methods (see Discussion). Because all TACs were simulated consistent with the 1T model, $t^*$ was set to 0 for $MRTM_O$, MRTM, and MRTM2. The first time point was excluded from fitting, however, to minimize any bias introduced by the integral(s) on the right-hand sides of the operational equations. For SRTM, SRTM2, and 1TKA, the initial parameter values were chosen randomly from the range of 75 to 125% of the true parameter value. To calculate $BP$ and $R_1$ for 1TKA, the true values of $K_1'$ and $k_2'$ were used for consistency with the use of noise-free $C'(t)$ in the reference tissue methods. Parameter estimates were considered outliers if $BP$ or $R_1$ values were less than zero or more than five times the true values, which should include nonconvergence cases. Bias was expressed as percent deviation of the sample mean from the true value and the variability was calculated as percent sample SD relative to the true value excluding outliers. Theoretical $BP$ and $R_1$ variability were calculated as percent C-R SD relative to the true value.

For MRTM2 and SRTM2, $k_2'$ will be estimated by preliminary application of MRTM or SRTM to ROI TACs. To assess the magnitude of noise in this ROI-based $k_2'$ estimation, 1,000 noisy tissue TACs were generated at noise levels ranging from 1 to 7%, which would cover a range of TAC noise found in large to small ROIs. $k_2'$ was estimated by MRTM, with sample bias and sample variability of $k_2'$ calculated as above. In addition, the effect of error in $k_2'$ estimates on MRTM2 estimation of $BP$ and $R_1$ was evaluated by calculating the bias of $BP$ and $R_1$ estimates by fitting the original gray matter TACs using biased $k_2'$ values (ranging from −6 to +6%). All simulation analyses were performed in MATLAB (The MathWorks, Natick, MA, U.S.A.), or pixel-wise kinetic modeling (PMOD) software (PMOD Group, Zurich, Switzerland).

## Positron emission tomography study analysis

The original reconstructed PET data were corrected for subject motion by registering each frame to a summed image of all frames, and the summed PET image was coregistered to a T1-weighted magnetic resonance image (repetition time/echo time = 21/9.2 milliseconds), acquired on a 1.5-T Phillips Intera (Phillips Medical Systems, Best, The Netherlands), in both cases using a six-parameter mutual information registration technique (Jenkinson et al., 2002) in the image analysis software MEDx (Sensor Systems Inc., Sterling, Virginia, U.S.A).

**TABLE 2.** *One-tissue-compartment kinetic parameter values used for simulating time–activity curves*

| Region | $K_1$ ($mL \cdot min^{-1} \cdot mL^{-1}$) | $k_2$ ($min^{-1}$) | $BP$ | $R_1$ |
|---|---|---|---|---|
| Cerebellum* | 0.615 | 0.056 | — | — |
| Raphe | 0.496 | 0.013 | 2.55 | 0.81 |
| Striatum | 0.656 | 0.023 | 1.64 | 1.07 |
| Thalamus | 0.662 | 0.021 | 1.91 | 1.08 |
| Frontal cortex | 0.697 | 0.050 | 0.27 | 1.13 |
| White matter | 0.260 | 0.022 | 0.09 | 0.42 |

* The $K_1$ and $k_2$ values for cerebellum (reference region) refer to those of $K_1'$ and $k_2'$, respectively.

The summed PET image was then fused with the coregistered magnetic resonance image using an image fusion tool in PMOD. Several anatomical ROIs were manually defined on this fused image, and ROI TACs from the cerebellum (~400 voxels, voxel size = 3.4 × 3.4 × 3.4 mm), raphe (~40 voxels), striatum (~110 voxels), thalamus (~90 voxels), frontal cortex (~400 voxels), and white matter (~200 voxels) were obtained. These ROI TACs were fitted by 1TKA using individual metabolite-corrected plasma input functions. The mean 1TKA parameter values from five of eight subjects were used to generate noise-free TAC data, as described in the previous section regarding simulation analysis.

To compare voxel-wise *BP* and $R_1$ estimates between the different reference tissue models as well as 1TKA, individual-voxel TACs were obtained from the raphe, striatum, and frontal cortex. MRTM2 and SRTM2 require *a priori* knowledge of value, which was provided by preliminary application of MRTM. To minimize the variability of estimation by MRTM (see the simulation results), a weighted (according to ROI size) mean value estimated from ROI TACs of raphe, striatum, and thalamus was used. To calculate *BP* and $R_1$ for 1TKA, the values of $k_2'$ and $K_1'$ estimated by 1TKA for the cerebellar ROI were used. Parameter estimate outliers were arbitrarily defined as *BP* or $R_1$ values less than zero or more than five times the same values used in the simulation analysis.

For comparison to simulations, percent ROI and voxel TAC noise was calculated based on deviations from 1TKA fitting for the latter portion of the TAC (50 to 90 minutes). ROI noise values [mean ± SD (range)] were 3.1 ± 1.0% (2.1–4.9%), 1.9 ± 0.5% (1.1–2.3%), 2.4 ± 0.6% (1.2–2.8%) and 2.6 ± 0.6% (1.8–3.1%) in the raphe, striatum, thalamus, and frontal cortex, respectively. Voxel noise values were 12 ± 4%, 11 ± 4%, 15 ± 5%, and 23 ± 8% in the raphe, striatum, frontal cortex, and white matter, respectively. If the actual scan data had been acquired with the doubled sampling rate, as used in the simulation, all these noise values would have increased by a factor of $\sqrt{2}$. Thus, for comparison to the simulations, the percent noise values in the actual PET data were multiplied by $\sqrt{2}$. Thus, ROI noise values of 3 to 7%, 2 to 3%, 2 to 4%, and 2 to 4% in the raphe, striatum, thalamus, and frontal cortex, respectively, and voxel noise values of 15% and 30% for gray and white matter, respectively, were chosen as typical noise levels in evaluating the simulation results.

Comparison of estimates between MRTM and 1TKA as well as comparison of voxel-based *BP* and $R_1$ estimates between all methods were made by performing paired *t*-tests. Statistical significance was defined as $P < 0.05$.

Parametric images of *BP* and $R_1$ were generated from the motion-corrected data sets (n = 8) by $MRTM_O$ (*BP* only), MRTM2, SRTM2, and SRTM, respectively. The SRTM and SRTM2 parametric imaging was performed based on the basis function method of Gunn et al. (1997) to improve processing speed. All parametric imaging was performed in PMOD installed on a PC workstation (Dell Computer Co., Austin, TX, U.S.A., 1.7 GHz Pentium IV/1 GB-RAM running Microsoft Windows 2000, Microsoft Co., Redmond WA, U.S.A). PMOD is platform-independent software programmed in Java environment (Mikolajczyk et al., 1998).

## RESULTS

### Simulation analysis

**[$^{11}$C]DASB time–activity curves.** The cerebellum TAC and frontal cortex TAC with a low *BP* (0.27) had the earliest peaks (Fig. 1A), whereas the striatum (1.64), thalamus (1.91), and raphe (2.55) TACs peaked later. The white matter TAC with a very low *BP* (0.09) increased slowly, peaked late, and reached the level of the cerebellum or frontal cortex by 75 to 90 minutes. Even with high radioligand delivery (Table 2), the [$^{11}$C]DASB TACs were slow to reach their peaks because of the relatively high distribution volumes. The noisy striatal TACs (Fig. 1B) showed considerably more variability at later time points, as produced by Eq. 7.

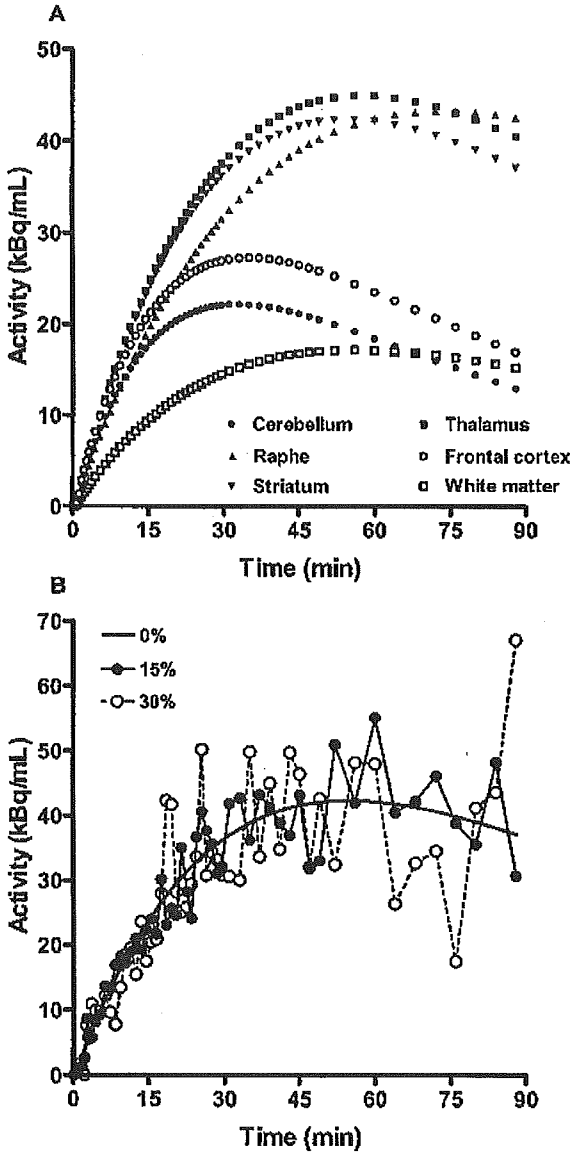


FIG. 1. Simulated [$^{11}$C]DASB noise-free time–activity curves (**A**) and examples of noise-added time–activity curves for the striatum at noise levels 0%, 15%, and 30% (**B**).

***BP* estimation.** Table 3 shows *BP* percent bias and variability by all methods for simulated data at different noise levels in the raphe, striatum, and frontal cortex,

and Fig. 2 depicts the bias (Fig. 2A) and variability (Fig. 2B) for the three gray matter regions together at the typical gray matter noise level of 15%. The three-parameter methods, MRTM and SRTM, had very similar characteristics. The two-parameter versions, MRTM2 and SRTM2, were also similar. SRTM2 and the two-parameter 1TKA produced identical parameter estimates to three significant digits (Table 3; see Discussion). MRTM2, SRTM2, and 1TKA all had the smallest magnitude of bias due to noise (1–4%, Fig. 2A). The variability for these three methods (12–20%, Fig. 2B), however, was somewhat higher than that of $MRTM_O$ but was substantially lower than that of MRTM or SRTM. Note that the two-parameter methods had the advantage over the other three-parameter methods of exact knowledge of the $k_2'$ value. Regionally, the percent variability for the two-parameter methods was larger in the high-*BP* raphe and the low-*BP* frontal cortex, and somewhat lower in the intermediate-*BP* striatum. These sample variability values showed good agreement with the predicted C-R values (Table 3), except at the highest noise levels in the raphe. There were no outliers for the two-parameter methods except for a few at the highest noise levels (Table 3). Overall, *BP* estimates by MRTM2 and SRTM2 were effectively identical, with mean percent-*BP* differences between the two models over 1,000 runs at 15% noise of 0 ± 1%, 0 ± 1%, and 1 ± 6% for raphe, striatum, and frontal cortex, respectively.

$MRTM_O$ had the largest magnitude of bias (−12 to −70%, Fig. 2A), but the smallest variability (4–14%, Fig 2B), and no outliers except at the highest noise level (Table 3). MRTM and SRTM, had magnitudes of bias intermediate between $MRTM_O$ and MRTM2, SRTM2, or 1TKA (−20%, Fig. 2A), the largest variability (40–70%, Fig. 2B), and large numbers of outliers up to 10% at 15% noise (Table 3). Unlike MRTM2, SRTM2, or 1TKA, the variability values for MRTM and SRTM showed a noticeable discrepancy from the C-R values, even at moderate noise levels (see Discussion). However, this discrepancy artifactually appeared to decrease with increasing number of outliers because the variability values were calculated excluding the outliers (Table 3). The

**TABLE 3.** *Bias and variability of binding potential* (BP) *estimates by six different models for simulated [$^{11}$C]DASB data at different noise levels*

| | $MRTM_O$ | | | MRTM | | | SRTM | | | | MRTM2 | | | SRTM2/1TKA | | | |
|---|---|---|---|---|---|---|---|---|---|---|---|---|---|---|---|---|---|
| Noise (%) | Bias (%) | Variability (%) | N* | Bias (%) | Variability (%) | N* | Bias (%) | Variability (%) | C-R (%) | N* | Bias (%) | Variability (%) | N* | Bias (%) | Variability (%) | C-R (%) | N* |
| Raphe ("true" *BP* value of 2.55) | | | | | | | | | | | | | | | | | |
| 0 | 0.0 | 0 | 0 | −0.1 | 0 | 0 | −0.1 | 0 | — | 0 | −0.1 | 0 | 0 | 0.0 | 0 | — | 0 |
| 5 | −55.4 | 7.5 | 0 | 5.2 | 20.3 | 0 | 5.1 | 20.4 | 15.5 | 0 | 0.6 | 5.9 | 0 | 0.7 | 6.0 | 5.9 | 0 |
| 10 | −66.7 | 3.5 | 0 | 15.8 | 52.1 | 29 | 15.3 | 52.5 | 31.1 | 28 | 1.6 | 12.0 | 0 | 1.6 | 12.3 | 11.7 | 0 |
| 15 | −69.4 | 2.9 | 0 | 21.4 | 70.9 | 83 | 20.7 | 72.0 | 46.6 | 79 | 3.6 | 20.1 | 0 | 3.6 | 20.5 | 17.6 | 0 |
| 20 | −70.5 | 3.1 | 0 | 17.7 | 75.3 | 158 | 15.6 | 74.5 | 62.1 | 153 | 4.8 | 27.5 | 0 | 4.7 | 28.0 | 23.5 | 0 |
| 25 | −71.6 | 3.7 | 0 | 16.6 | 79.5 | 238 | 14.6 | 81.5 | 77.7 | 227 | 9.9 | 40.4 | 1 | 9.7 | 40.9 | 29.3 | 1 |
| 30 | −72.5 | 4.7 | 0 | 9.9 | 78.2 | 278 | 6.2 | 78.1 | 93.2 | 263 | 14.1 | 51.4 | 6 | 13.7 | 51.7 | 35.2 | 6 |
| Striatum ("true" *BP* value of 1.64) | | | | | | | | | | | | | | | | | |
| 0 | −0.1 | 0 | 0 | −0.1 | 0 | 0 | 0.0 | 0 | — | 0 | −0.1 | 0 | 0 | 0.0 | 0 | — | 0 |
| 5 | −32.6 | 6.0 | 0 | 2.7 | 11.1 | 0 | 2.6 | 11.1 | 9.4 | 0 | 0.3 | 3.9 | 0 | 0.3 | 4.0 | 4.0 | 0 |
| 10 | −42.1 | 3.5 | 0 | 10.7 | 37.8 | 15 | 10.0 | 38.4 | 18.8 | 14 | 0.7 | 7.9 | 0 | 0.7 | 8.0 | 7.9 | 0 |
| 15 | −44.5 | 3.7 | 0 | 14.8 | 47.3 | 56 | 13.7 | 49.9 | 28.3 | 51 | 1.0 | 11.8 | 0 | 0.9 | 12.0 | 11.9 | 0 |
| 20 | −45.6 | 4.5 | 0 | 17.8 | 63.7 | 105 | 13.7 | 60.4 | 37.7 | 101 | 1.7 | 16.8 | 0 | 1.5 | 17.2 | 15.8 | 0 |
| 25 | −46.6 | 5.4 | 0 | 18.6 | 68.0 | 172 | 13.2 | 65.0 | 47.1 | 161 | 4.8 | 22.8 | 0 | 4.6 | 23.4 | 19.8 | 0 |
| 30 | −47.3 | 6.6 | 0 | 13.4 | 74.5 | 184 | 5.3 | 68.4 | 56.5 | 166 | 6.3 | 27.1 | 0 | 5.8 | 27.5 | 23.7 | 0 |
| Frontal cortex ("true" *BP* value of 0.27) | | | | | | | | | | | | | | | | | |
| 0 | −0.1 | 0.0 | 0 | −0.1 | 0 | 0 | 0.0 | 0 | — | 0 | −0.1 | 0.0 | 0 | 0.0 | 0 | — | 0 |
| 5 | −11.4 | 4.7 | 0 | 11.6 | 41.3 | 42 | 6.7 | 35.6 | 12.8 | 31 | 0.1 | 6.9 | 0 | 0.1 | 6.8 | 6.8 | 0 |
| 10 | −11.8 | 8.7 | 0 | 11.3 | 61.7 | 100 | 3.3 | 51.8 | 25.7 | 61 | 1.2 | 14.1 | 0 | 1.0 | 14.1 | 13.5 | 0 |
| 15 | −11.9 | 13.5 | 0 | 2.1 | 59.0 | 106 | −4.5 | 39.6 | 38.5 | 48 | 1.4 | 20.7 | 0 | 1.0 | 20.4 | 20.3 | 0 |
| 20 | −12.1 | 18.0 | 0 | 6.5 | 71.1 | 113 | −5.2 | 41.9 | 51.4 | 49 | 2.6 | 27.8 | 0 | 1.9 | 27.4 | 27.0 | 0 |
| 25 | −12.3 | 22.4 | 0 | 5.5 | 68.3 | 144 | −4.3 | 48.5 | 64.2 | 46 | 4.1 | 35.1 | 0 | 3.0 | 34.6 | 33.8 | 0 |
| 30 | −12.6 | 26.8 | 2 | 10.7 | 79.0 | 162 | −5.4 | 44.2 | 77.1 | 57 | 6.5 | 42.1 | 4 | 4.6 | 41.8 | 40.5 | 2 |

Bias and variability are expressed as mean percent deviation of *BP* from the true value and percent SD of sample excluding outliers ($n \leq 1{,}000$) relative to the true *BP* value, respectively. SRTM2 and 1TKA have identical estimation characteristics in this simulation.

* N indicates the number of outliers.

C-R, theoretical variability values of *BP* estimates as predicted by the Cramer-Rao lower bound; $MRTM_O$, MRTM, MRTM2, original multilinear reference tissue model, its rearranged three-parameter model and two parameter model, respectively; SRTM, SRTM2, simplified reference tissue model and its two-parameter model, respectively; 1TKA, one-tissue kinetic analysis.

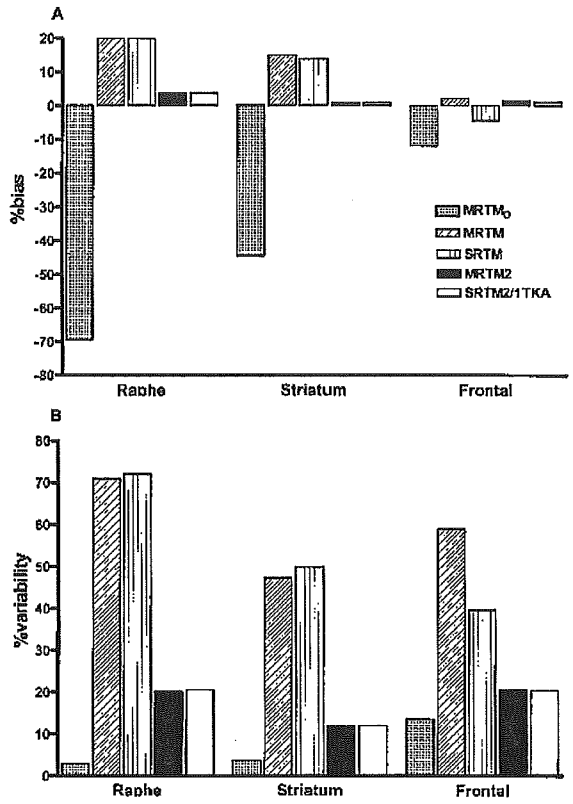


**FIG. 2.** Bias (**A**) and variability (**B**) of *BP* estimates by six different models using simulated [$^{11}$C]DASB time–activity curves for raphe, striatum, and frontal cortex at 15% noise. SRTM2 and 1TKA have identical estimation characteristics in this simulation. MRTM$_O$, MRTM, and MRTM2 indicate original multilinear reference tissue model, its rearranged three-parameter model and two-parameter model, respectively; *BP*, binding potential; SRTM and SRTM2, simplified reference tissue model and its two-parameter model, respectively; 1TKA, one-tissue compartment kinetic analysis.

bias and variability were similar for MRTM and SRTM in both the striatum and raphe. However, in the frontal cortex, MRTM had somewhat larger variability than SRTM, with more outliers at all noise levels (Table 3).

Thus, MRTM2, SRTM2 and 1TKA, given knowledge of $k_2'$ all markedly reduced the magnitude of *BP* bias compared with MRTM$_O$ at the expense of somewhat increased variability. Furthermore, these methods considerably reduced *BP* bias in the high-*BP* regions and *BP* variability in all regions by a factor of two or three compared with MRTM or SRTM (Table 3).

For the white matter, however, *BP* estimation tended to be unstable for all methods, particularly for MRTM$_O$, MRTM, and SRTM. For example, at the typical white matter noise level, *BP* estimates were all negative for MRTM$_O$, whereas the mean ± SD (range) values of *BP* estimates over 1,000 runs for SRTM, MRTM2, and SRTM2/1TKA were −0.10 ± 6.48 (−168 to +93), 0.14 ± 0.22 (−0.29 to +2.08), and 0.13 ± 0.23 (−0.30 to +2.08), respectively. This instability of *BP* estimation in the white matter suggested that parametric images from these latter methods will contain some white matter voxels with inappropriately high positive *BP* values, due simply to statistical noise in the data. For example, histograms of *BP* estimates for MRTM2 and SRTM are shown in Fig. 3A, where 1% and 5% of voxels had *BP* values >1, respectively. Although the *BP* in the white matter is not generally of pathophysiologic interest, parametric images with noisy white matter voxels could be visually misleading.

**$R_1$ estimation.** Table 4 shows the bias and variability of $R_1$ estimates at different noise levels in the raphe, striatum, and frontal cortex, and Fig. 4 depicts the bias (Fig. 4A) and variability (Fig. 4B) for the gray matter regions at 15% noise. MRTM2, SRTM2, and 1TKA all had the smallest magnitudes of bias (<0.3% for all noise levels and gray matter regions), as well as the smallest variability (<6%, Fig. 4B), at least a factor of 2 lower than SRTM, and no outliers (Table 4). The variability values were in close agreement with the C-R bounds. These $R_1$ bias and variability values were considerably

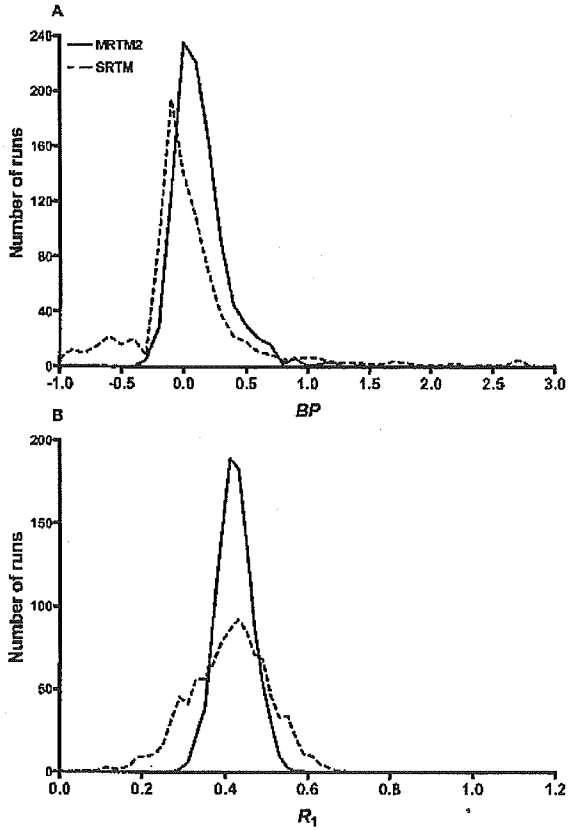


**FIG. 3.** Histograms of estimated *BP* (**A**) and $R_1$ (**B**) by MRTM2 and SRTM for simulated white matter time–activity curves at 30% noise (1,000 runs). *BP*, binding potential; $R_1$, relative delivery; MRTM2, two-parameter multilinear reference tissue model; SRTM, simplified reference tissue model.

**TABLE 4.** *Bias and variability of relative delivery ($R_1$) estimates by five different models for simulated [$^{11}$C]DASB data at different noise levels*

| | MRTM | | | SRTM | | | | MRTM2 | | | SRTM2/1TKA | | | |
|---|---|---|---|---|---|---|---|---|---|---|---|---|---|---|
| Noise (%) | Bias (%) | Variability (%) | N* | Bias (%) | Variability (%) | C-R (%) | N* | Bias (%) | Variability (%) | N* | Bias (%) | Variability (%) | C-R (%) | N* |
| Raphe ("true" $R_1$ value of 0.81) | | | | | | | | | | | | | | |
| 0 | 0.0 | 0 | 0 | 0.0 | 0.0 | — | 0 | 0.0 | 0.0 | 0 | 0.0 | 0.0 | — | 0 |
| 5 | 0.0 | 3.4 | 0 | −0.1 | 3.4 | 3.5 | 0 | 0.1 | 1.5 | 0 | 0.1 | 1.6 | 1.6 | 0 |
| 10 | −0.1 | 7.1 | 0 | −0.4 | 7.0 | 7.0 | 0 | 0.0 | 3.1 | 0 | 0.0 | 3.2 | 3.1 | 0 |
| 15 | 0.1 | 10.2 | 0 | 0.1 | 10.6 | 10.5 | 0 | 0.1 | 4.5 | 0 | 0.2 | 4.7 | 4.7 | 0 |
| 20 | 0.6 | 13.6 | 0 | −0.5 | 14.1 | 14.0 | 0 | −0.1 | 5.9 | 0 | 0.0 | 6.1 | 6.2 | 0 |
| 25 | 0.2 | 16.9 | 0 | −0.7 | 17.0 | 17.5 | 0 | −0.5 | 7.5 | 0 | −0.4 | 7.7 | 7.8 | 0 |
| 30 | 0.6 | 20.3 | 0 | 0.3 | 20.3 | 21.0 | 0 | −0.4 | 8.9 | 0 | −0.1 | 9.3 | 9.3 | 0 |
| Striatum ("true" $R_1$ value of 1.07) | | | | | | | | | | | | | | |
| 0 | 0.0 | 0 | 0 | 0.0 | 0.0 | — | 0 | 0.0 | 0.0 | 0 | 0.0 | 0.0 | — | 0 |
| 5 | −0.1 | 3.4 | 0 | 0.0 | 3.4 | 3.4 | 0 | 0.1 | 1.6 | 0 | 0.1 | 1.6 | 1.6 | 0 |
| 10 | −0.2 | 6.7 | 0 | −0.3 | 6.8 | 6.8 | 0 | 0.1 | 3.1 | 0 | 0.1 | 3.3 | 3.2 | 0 |
| 15 | 0.2 | 9.7 | 0 | 0.1 | 10.4 | 10.2 | 0 | −0.1 | 4.7 | 0 | 0.0 | 4.9 | 4.8 | 0 |
| 20 | 0.8 | 13.0 | 0 | 0.0 | 13.1 | 13.6 | 0 | −0.2 | 6.3 | 0 | −0.1 | 6.6 | 6.4 | 0 |
| 25 | 1.6 | 15.5 | 0 | −1.8 | 17.3 | 17.0 | 0 | 0.2 | 7.8 | 0 | 0.5 | 8.2 | 8.0 | 0 |
| 30 | 2.7 | 18.0 | 0 | −1.0 | 20.8 | 20.4 | 0 | −0.1 | 9.4 | 0 | 0.3 | 9.8 | 9.6 | 0 |
| Frontal cortex ("true" $R_1$ value of 1.13) | | | | | | | | | | | | | | |
| 0 | 0.1 | 0 | 0 | 0.0 | 0.0 | — | 0 | 0.0 | 0.0 | 0 | 0.0 | 0.0 | — | 0 |
| 5 | 1.2 | 2.6 | 0 | −0.8 | 3.8 | 3.4 | 0 | −0.1 | 2.0 | 0 | −0.1 | 2.0 | 2.0 | 0 |
| 10 | 3.0 | 4.2 | 0 | −3.3 | 11.4 | 6.8 | 5 | −0.1 | 4.0 | 0 | 0.0 | 4.0 | 3.9 | 0 |
| 15 | 3.4 | 5.5 | 0 | −4.1 | 17.9 | 10.2 | 18 | 0.1 | 5.8 | 0 | 0.3 | 5.9 | 5.9 | 0 |
| 20 | 3.9 | 6.4 | 0 | −4.4 | 23.0 | 13.6 | 27 | 0.0 | 7.6 | 0 | 0.4 | 7.8 | 7.8 | 0 |
| 25 | 4.0 | 7.7 | 0 | −3.7 | 27.8 | 17.0 | 31 | −0.4 | 9.7 | 0 | 0.3 | 10.0 | 9.8 | 0 |
| 30 | 3.7 | 9.2 | 0 | −4.0 | 28.6 | 20.4 | 45 | −0.6 | 11.7 | 0 | 0.3 | 12.1 | 11.8 | 0 |

Bias and variability are expressed as mean percent deviation of $R_1$ from the true value and percent SD of sample excluding outliers ($n \leq 1{,}000$) relative to the true $R_1$ value, respectively. SRTM2 and 1TKA have identical estimation characteristics in this simulation.

* N indicates the number of outliers.

C-R, theoretical variability of $R_1$ estimates as predicted by the Cramer-Rao lower bound; MRTM, MRTM2, multilinear reference tissue model, its rearranged three-parameter model and two parameter model, respectively; the original multilinear reference tissue model ($MRTM_O$), which is unstable for $R_1$ estimations in the present simulations, is not included in Table 4); SRTM, SRTM2, simplified reference tissue model and its two-parameter model, respectively; 1TKA, one-tissue kinetic analysis.

smaller than the corresponding values for *BP* estimations (Table 3). As was the case for *BP* estimates, $R_1$ estimates by MRTM2 and SRTM2 were virtually identical, with percent differences between the two models over 1,000 runs of 0.1 ± 0.4%, −0.1 ± 0.6%, and 0.4 ± 1.0% for raphe, striatum, and frontal cortex, respectively; and $R_1$ estimates by SRTM2 and 1TKA were identical to three significant digits (see Discussion).

Both MRTM and SRTM had slightly larger magnitudes of bias (up to 4%, Fig. 4A) and higher variability by a factor of two or three (Fig. 4B) than did MRTM2, SRTM2, or 1TKA, except that MRTM had variability in the frontal cortex comparable with that for MRTM2, SRTM2, or 1TKA (see Discussion). However, $MRTM_O$ $R_1$ estimation (data not shown) was very unstable, with outliers exceeding 50% at 15% noise and beyond for all gray matter regions.

Finally, for the white matter, unlike *BP* estimates, $R_1$ estimates by MRTM, SRTM, MRTM2, SRTM2 and 1TKA were stable with no outliers, as shown in the histogram for SRTM and MRTM2 in Fig. 3B.

Fig. 5 shows the correlation scatterplot between the MRTM2 parameter estimates $\gamma_1$ and $\gamma_2$ from the 1,000 simulated realizations in the three gray matter regions and white matter. For convenience of scale and interpretation, the parameters have been divided by $k_2'$ so the x and y axes are $R_1$ and $k_2/k_2'$, respectively. For a given region, the parameter estimates are correlated; this is reflected in the nonzero slope of the elliptical cloud of parameter estimates. For example, for voxels with lower than average $R_1$, the estimated $k_2$ also tended to be lower than the mean, resulting in increased values of *BP*. For white matter values, the spread of voxel noise produces a wide range of *BP* values with a long positive tail (Fig. 3A). The correlation plot in Fig. 5 suggested that appropriate thresholds using estimated $R_1$ and *BP* values might lead to an algorithm that would eliminate the potentially misleading voxels in white matter with high *BP* values produced by noise. For example, the simplest approach would be to assign a *BP* value of zero to all voxels with $R_1$ values below a certain cutoff value, which might result in cosmetically more satisfactory parametric *BP*

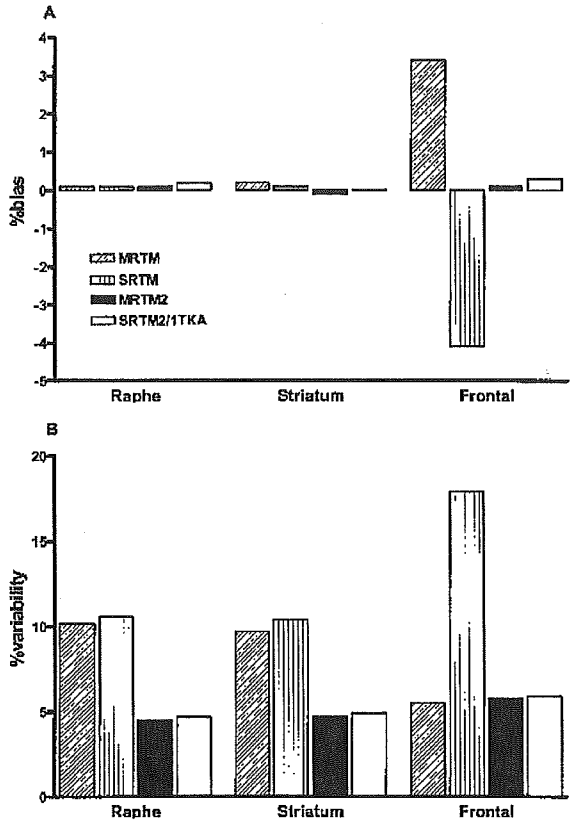


**FIG. 4.** Bias (**A**) and variability (**B**) of $R_1$ estimates by five different models using simulated [$^{11}$C]DASB time–activity curves for raphe, striatum, and frontal cortex at 15% noise. SRTM2 and 1TKA have identical estimation characteristics in this simulation. $R_1$, relative delivery; MRTM and MRTM2, rearranged three-parameter model and its two-parameter model, respectively; SRTM and SRTM2, simplified reference tissue model and its two-parameter model, respectively; 1TKA, one-tissue compartment kinetic analysis.

images by removing these noise-induced high positive *BP* values within the white matter. The correlation scatter plot in Fig. 5 was virtually identical to that for SRTM2 (data not shown).

**$k_2'$ estimation.** MRTM2 and SRTM2 require *a priori* estimation of $k_2'$. Here, we propose determination of $k_2'$ by MRTM or SRTM applied to ROI data. Table 5 shows the simulated bias and variability of $k_2'$ estimates by MRTM at different noise levels in the raphe, striatum, thalamus, and frontal cortex. At typical ROI noise levels in the striatum and thalamus (2–4%), the magnitude of bias was very small (<0.9%), and the variability was moderate (< 13%) (Table 5). In the frontal cortex (2–4% noise) and raphe (3–7% noise), the magnitude of bias was larger (raphe: ~1.9%, frontal cortex: ~10%), and the variability was larger (raphe: ~19%, frontal cortex: ~44%) (Table 5). Thus, these results suggested that averaging of several $k_2'$ samples from high-*BP* ROIs might be required to minimize the variability of $k_2'$ estimation. For example, assuming $k_2'$ estimates from different ROIs were statistically independent and assuming the average noise level for each ROI, a weighted mean $k_2'$ from raphe, striatum, and thalamus (weighted by the inverse of the variance) would have variability of less than 6%.

Error in the estimated value for each subject introduces bias in all the *BP* and $R_1$ estimates for that subject. The magnitudes of MRTM2 bias in *BP* estimates due to biased $k_2'$ estimates were 0.9, 0.4, and 0.1 times the bias of $k_2'$ estimates for raphe, striatum, and frontal cortex, respectively (Fig. 6A). The corresponding magnitudes of bias in $R_1$ estimates were smaller (i.e., 0.3, 0.2, and 0.04 times the bias of $k_2'$ estimates; Fig. 6B). Thus, small biases $k_2'$ estimates by MRTM for MRTM2 analysis would not result in any larger biases of *BP* or $R_1$ estimates. The effects of biased $k_2'$ on SRTM2 were identical to those of MRTM2 (data not shown).

## Positron emission tomography study analysis

**Comparison of voxel-wise *BP* and $R_1$ between models.** Fig. 7 depicts the mean regional *BP* (Fig. 7A) and $R_1$ (Fig. 7B) values estimated voxel-wise by different methods in eight [$^{11}$C]DASB PET studies. As predicted by the simulation analysis, the MRTM2 *BP* values were nearly identical to the SRTM2 *BP* values (Fig. 7A), with percent differences between the two models of 0.2 ± 0.6%, 0.1 ± 0.2%, and 0.2 ± 1% for raphe, striatum, and frontal cortex, respectively. The MRTM2 *BP* values were

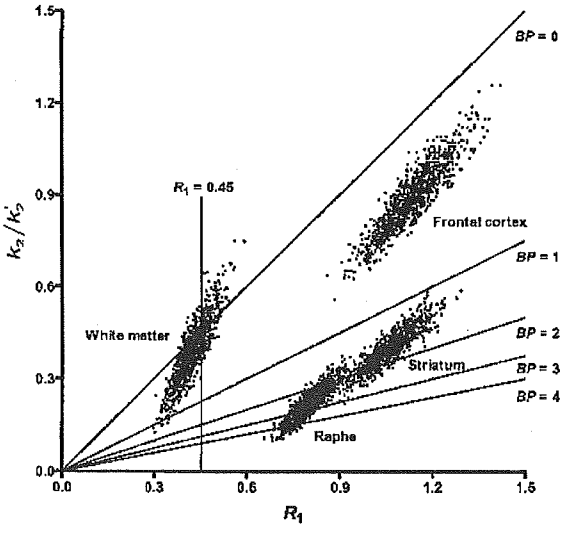


**FIG. 5.** Relationship between $R_1$ and *BP* estimates by MRTM2 for the three gray matter regions and white matter on a ($k_2/k_2'$) versus $R_1$ plot, where $k_2$ values were estimated from the second parameter in Eq. 3 as $k_2 = -\gamma_2$. Oblique straight lines indicate identical lines of different *BP* values (0, 1, 2, 3, and 4) calculated from the relationship $k_2/k_2' = R_1/(BP + 1)$. Because positively higher *BP* values in the white matter have lover $R_1$ values, assigning a *BP* value of zero to those voxels with low $R_1$ values (e.g., $R_1 = 0.45$ [vertical line]) would eliminate most of high positive *BP* values in the white matter. MRTM2, two-parameter multilinear reference tissue model; *BP*, binding potential; $R_1$, relative delivery.

**TABLE 5.** *Bias and variability of $k_2'$ estimates by three-parameter multilinear reference tissue model for simulated [$^{11}$C]DASB region-of-interest data at differnt noise levels*

| | Raphe | | Striatum | | Thalamus | | Frontal cortex | |
|---|---|---|---|---|---|---|---|---|
| Noise (%) | Bias (%) | Variability (%) | Bias (%) | Viarability (%) | Bias (%) | Variability (%) | Bias (%) | Variability (%) |
| 0 | 0.0 | 0.0 | 0.1 | 0.0 | 0.1 | 0.0 | 0.1 | 0.0 |
| 1 | 0.0 | 2.7 | 0.0 | 3.2 | 0.1 | 3.2 | −1.3 | 16.9 |
| 2 | 0.0 | 5.4 | 0.1 | 6.7 | 0.4 | 6.4 | −4.8 | 31.6 |
| 3 | 0.4 | 8.2 | 0.5 | 9.8 | 0.8 | 9.4 | −10.3 | 44.4 |
| 4 | 0.4 | 11.1 | 0.3 | 13.4 | 0.9 | 12.5 | −18.7 | 68.2 |
| 5 | 1.1 | 13.7 | 1.1 | 16.6 | 0.2 | 15.2 | −31.9 | 81.8 |
| 6 | 1.8 | 16.1 | 1.8 | 19.5 | 1.2 | 18.0 | −53.7 | 132 |
| 7 | 1.9 | 18.9 | 1.0 | 22.7 | 0.3 | 21.2 | −55.1 | 143 |

Bias and variability are expressed as mean percent deviation of $k_2'$ from the true value and percent SD of the sample (n = 1,000) relative to the true $k_2'$ value (0.056 min$^{-1}$), respectively.

similar to the 1TKA *BP* values (Fig. 7A), with percent differences between the two models of 4 ± 13%, 1 ± 6%, and 1 ± 4% for raphe, striatum, and frontal cortex, respectively. The intersubject coefficients of variation were calculated for *BP* and $R_1$ in raphe, striatum, and frontal cortex. The values for 1TKA and MRTM2 were comparable, with MRTM2 values smaller in four of six cases (Fig. 7A).

The mean *BP* values estimated by MRTM were similar to those estimated by SRTM for raphe and striatum (Fig. 7A), with respective percent differences between the two models of 1 ± 3% and 2 ± 2%. However, the MRTM *BP* values for frontal cortex were somewhat higher (12%) than the corresponding SRTM *BP* values. The mean *BP* values estimated by MRTM or SRTM were higher (by ~16% and ~18% in the raphe and striatum, respectively) than those estimated by MRTM2 (Fig. 7A). These between-method *BP* differences were consistent with the simulations, where percent *BP* bias differences between MRTM and MRTM2 were ~18% and ~14% in the raphe and striatum, respectively; and the differences between MRTM and SRTM in the frontal cortex was ~7% (Table 3).

The mean *BP* values estimated by $MRTM_O$ were strikingly lower by 76%, 44%, and 22% in the raphe, striatum, and frontal cortex, respectively, than those estimated by MRTM2 (Fig. 7A). These *BP* differences between $MRTM_O$ and MRTM2 were also consistent with the simulation results, where percent *BP* bias differences between the two models were ~73%, ~46%, and ~13% in the raphe, striatum, and frontal cortex, respectively (Table 3).

Voxel *BP* outliers represented sizable percentages for both MRTM and SRTM (27%, 6%, and 15% of voxels in the raphe, striatum, and frontal cortex, respectively). However, there were no outliers for $MRTM_O$, MRTM2, SRTM2, or 1TKA, as predicted by the simulations. The number of outliers for MRTM and SRTM was larger than that predicted by the simulations, particularly for raphe (Table 3). This increased outlier percentage for MRTM and SRTM was due to increased number of low (negative) *BP* values, where the low-to-high outlier ratios were approximately three times those in the simulations, and may be a result of partial volume effects inherent in the actual PET data.

As predicted by the simulations, the MRTM2 $R_1$ values were effectively identical to the SRTM2 $R_1$ values (Fig. 7B), with percent differences between the two models of 0.0 ± 0.1%, −0.3 ± 0.1%, and −0.3 ± 0.2% for raphe, striatum, and frontal cortex, respectively. As was the case for *BP*, the MRTM2 $R_1$ values were similar to the 1TKA $R_1$ values (Fig. 7B), with percent differences between the two models of 0.5 ± 3.0%, 0.0 ± 3.0%, and 0.1 ± 1.0% for raphe, striatum, and frontal cortex, respectively. The mean $R_1$ values estimated by MRTM were similar within 2% to those estimated by SRTM for raphe and striatum. However, the MRTM $R_1$ values for frontal cortex were somewhat higher (10%) than the corresponding SRTM $R_1$ values. The mean $R_1$ values estimated by MRTM or SRTM were higher (~5% in the raphe) and lower (~5% in the striatum) than those estimated by MRTM2 (Fig. 7B). These $R_1$ differences between MRTM and SRTM were consistent with the simulations, where the respective percent $R_1$ bias differences were <1% in both the raphe and striatum and ~8% in the frontal cortex, respectively. However, these $R_1$ differences between MRTM or SRTM and MRTM2 in the raphe and striatum were slightly larger compared with the simulations, where the corresponding percent $R_1$ bias differences were <1% (Table 4). $MRTM_O$ was very unstable for $R_1$ estimation with large percentages of outliers exceeding 50% (data not shown), as was the case in the simulations. There were no outliers of $R_1$ estimates for the other models except for SRTM, where there were a small number of outliers (2%) in the frontal cortex but none in the raphe or striatum with the outlier percentage very consistent with the simulations (Table 4).

**$k_2'$ estimation.** The weighted mean $k_2'$ values estimated by MRTM from tissue ROI TACs including the raphe, striatum, and thalamus were 0.057 ± 0.004 min$^{-1}$. These

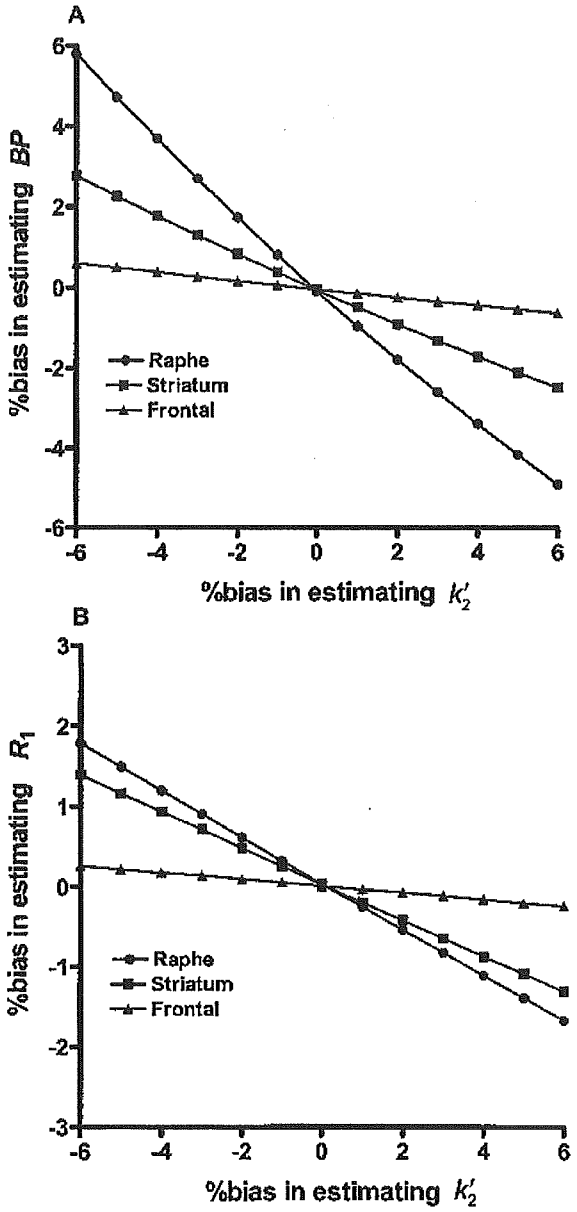


FIG. 6. Sensitivity of *BP* (A) and $R_1$ (B) estimation by MRTM2 to the bias of $k_1'$ estimates by MRTM. *BP*, binding potential; $R_1$, relative delivery; MRTM and MRTM2, rearranged three-parameter model and its two-parameter model, respectively.

MRTM $k_2'$ values were very similar to those estimated by 1T KA using the metabolite-corrected input functions ($0.058 \pm 0.007$ min$^{-1}$), with percent differences between MRTM and 1TKA of $-1 \pm 9\%$. These $k_2'$ values were used for voxel-wise *BP* and $R_1$ estimations by MRTM2 and SRTM2 as well as parametric image generation by MRTM2.

**Parametric images.** Figure 8 shows parametric images of *BP* and $R_1$ from one typical subject. The $MRTM_O$ and MRTM2 computations each required <15 seconds, whereas the basis function SRTM or SRTM2 required approximately 24 minutes to generate *BP* and $R_1$ parametric image sets of ~750,000 voxels each. The statistical quality of both *BP* and $R_1$ images by MRTM2 or SRTM2 is substantially better than the SRTM images, and the corresponding MRTM2 and SRTM2 images were effectively identical (Fig. 8), as expected from the simulation results. Noise in the $MRTM_O$ *BP* image is somewhat lower compared with the MRTM2 or SRTM2 *BP* image. However, those voxels with high *BP* values in the SRTM and MRTM2 or SRTM2 images show markedly lower *BP* values in the corresponding $MRTM_O$ image (Fig. 8). These observations were consistent with the simulations, in which $MRTM_O$ showed the smallest variability but a marked underestimation of *BP*. Also as suggested by the simulations, the *BP* image but not the $R_1$ image by MRTM2 or SRTM2 contained a few voxels with moderately high *BP* values in the white matter, whereas the corresponding *BP* image by SRTM

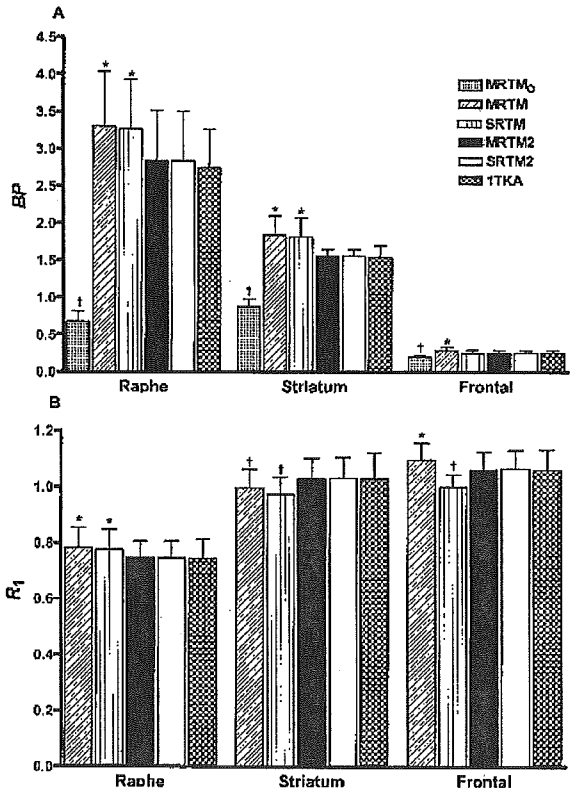


FIG. 7. Mean regional *BP* (A) and $R_1$ (B) estimated voxel-wise by six different models (excluding $MRTM_O$ for $R_1$) in eight [$^{11}$C]DASB PET studies. Error bars indicate SD. *Significantly ($P < 0.05$) lower compared with MRTM2, SRTM2, or 1TKA. *BP*, binding potential; $R_1$, relative delivery; $MRTM_O$, MRTM, and MRTM2, original multilinear reference tissue model, its rearranged three-parameter model and two-parameter model, respectively; SRTM and SRTM2, simplified reference tissue model and its two-parameter model, respectively; 1TKA, one-tissue compartment kinetic analysis.